Magnetically-Assisted 3D Bioprinting of Anisotropic Tissue-Mimetic Constructs

Alberto Pardo, Syeda Mahwish Bakht, Manuel Gomez-Florit, Ramón Rial, Rosa F. Monteiro, Simão P. B. Teixeira, Pablo Taboada, Rui L. Reis, Rui M. A. Domingues,* and Manuela E. Gomes*

Recreating the extracellular matrix organization and cellular patterns of aniso-tropic tissues in bioengineered constructs remains a significant biofabrication challenge. Magnetically-assisted 3D bioprinting strategies can be exploited to fabricate biomimetic scaffolding systems, but they fail to provide control over the distribution of magnetic materials incorporated in the bioinks while pre-serving the fidelity of the designed composites. To overcome this dichotomy, the concepts of magnetically- and matrix-assisted 3D bioprinting are combined here. By allowing low viscosity bioinks to remain uncrosslinked after printing, this approach enables the arrangement of incorporated magnetically-responsive microfibers without compromising the resolution of printed structures before inducing their solidification. Moreover, the fine design of these magnetic microfillers allows the use of low inorganic contents and weak magnetic field strengths, minimizing the potentially associated risks. This strategy is evalu-ated for tendon tissue engineering purposes, demonstrating that the synergy between the biochemical and biophysical cues stemming from a tendon-like anisotropic fibrous microstructure, combined with remote magneto-mechanical stimulation during in vitro maturation, is effective on directing the fate of the encapsulated human adipose-derived stem cells toward tenogenic pheno-type. In summary, the developed strategy allows the fabrication of anisotropic high-resolution magnetic composites with remote stimulation functionalities, opening new horizons for tissue engineering applications.

1. Introduction

Besides acting as structural support and anchorage for resi-dent cells, the physical properties of fibrous native extra-cellular matrices (ECMs) also exquisitely dictate several morphogenetic processes.[1,2] The com-plex anisotropic topography and hierar-chical structure of native ECMs not only provide tissues with highly-anisotropic mechanical properties, but also impact on cells response by regulating their spreading, migration and morphology, specific features that are highly tissue-dependent.[3] Among the wide range of different materials proposed to engi-neer biomimetic constructs analogous to native tissues, polymeric hydrogels are particularly appealing options due to their water-rich composition, high biocompatibility, and high tunability of their physical and chemical properties.[4,5] However, unlike most human tissues, which are characterized by anisotropic cell patterns and ECMs organized into hierarchical fibrillar structures ranging from the nano- to the macro-scale, bulk polymeric hydrogels have inherent iso-tropic architectures that limit their poten-tial to recreate the rich biophysical cues of living tissues.

Various fabrication strategies have been devised in order to engineer aniso-tropic tissues based on polymeric hydro-gels that recapitulate the complex architectures of their native counterparts by providing essential tissue-specific biophysical and biochemical cues,[6,7] these include, e.g., electrospinning[8] and freeze-casting[9] strategies, shear-[10] or electric-induced[11] arrangement of hydrogel nanofillers, the design of hybrid

A. Pardo, S. M. Bakht, M. Gomez-Florit, R. Rial, R. F. Monteiro,
S. P. B. Teixeira, R. L. Reis, R. M. A. Domingues, M. E. Gomes
3B's Research Group I3Bs – Research Institute on Biomaterials
Biodegradables and Biomimetics University of Minho Headquarters of
the European Institute of Excellence on Tissue Engineering and
Regenerative Medicine AvePark – Parque de Ciência e Tecnologia Zona
Industrial da Gandra Barco
Guimarães 4805-017, Portugal
E-mail: rui.domingues@i3bs.uminho.pt; megomes@i3bs.uminho.pt

A. Pardo, S. M. Bakht, M. Gomez-Florit, R. Rial, R. F. Monteiro,
S. P. B. Teixeira, R. L. Reis, R. M. A. Domingues, M. E. Gomes
ICVS/3B's – PT Government Associate Laboratory Braga
Guimarães, Portugal

A. Pardo, P. Taboada
Colloids and Polymers Physics Group and Health Research Institute
(IDIS)
University of Santiago de Compostela
Santiago de Compostela 15782, Spain

R. Rial
Soft Mater and Molecular Biophysics Group
Department of Applied Physics
University of Santiago de Compostela
Santiago de Compostela 15782, Spain

**ADVANCED
SCIENCE NEWS**

www.advancedsciencenews.com

**ADVANCED
FUNCTIONAL
MATERIALS**

www.afm-journal.de

constructs with degradable/porous components,[12] unidirectional compression[13] and ion diffusion[14] of hydrogels precursor solutions, or the bottom-up assembly of micrometric gels.[15] However, most of these strategies have limitations on the offered control over hydrogel's architecture and do not allow their further on-demand external actuation through non-invasive techniques.

In this point, the modification of polymeric hydrogels with magnetically-responsive nano- or microfillers has emerged as a promising approach not only for creating anisotropic ordered patterns within their structural networks, but also for providing the composites with additional remote response functionalities.[16] Besides microstructural patterning, the application of external magnetic fields on magnetic hydrogels can further be used for the programmed contactless magneto-mechanical stimulation of the encapsulated cells, during their in vitro maturation and after construct transplantation in vivo.[17–19] On the other hand, the combination of 3D (bio)printing technologies with magnetic hydrogel (bio)inks allows an impressive control over the resolution of the designed anisotropic constructs and a significantly improved versatility and reproducibility in comparison with the aforementioned fabrication methods.[20]

Different types of magnetic nanoparticles (MNPs), particularly iron oxide-based, have been widely used to provide polymeric hydrogels with magnetic properties and ordered microstructures.[21–24] However, because large concentrations of MNPs are typically required,[16] and their controlled arrangement within the composites is still challenging,[25] this strategy has limited potential for creating biocompatible anisotropic hydrogels of relevant clinical size (cm scale). In this way, the incorporation and orientation of pre-manufactured anisotropic fillers, such as polymeric fibers/rod-shaped structures modified with low amounts of superparamagnetic MNPs, has emerged in recent years as an interesting alternative to develop controlled microstructural patterns within these type of biomaterials.[23,24] However, an usually overlooked but not less important variable for TE applications is the design of MNPs that are capable of delivering high magnetic response. This key fabrication parameter would enable to decrease the content of magnetic material and the intensity of the required electromagnetic radiation to attain the desired magnetic response, two critical safety/toxicity factors that need to be minimized in order to increase the translational potential of magnetically-responsive biomaterials.[26,27]

As mentioned, the remote manipulation of magnetic fillers within hydrogels can be integrated with additive manufacturing technologies for the automated fabrication of biomimetic materials and living constructs with ordered hierarchical architectures. Termed as magnetically-assisted 3D (bio)printing, this concept consists on the simultaneous application of external magnetic fields on the (bio)inks during the printing process to control the distribution of magnetic materials within the manufactured constructions.[21,28,29] In the seminal application of this strategy, rotating magnetic gradients applied during extrusion-based printing were used to induce the biaxial alignment of the magnetic particles incorporated in polymeric resin inks, producing different bioinspired anisotropic composites.[28] The versatility of this strategy was also demonstrated on digital light processing setups.[30] Interestingly, in one of the very few examples where the concept of 3D bioprinting has been explored, collagen-agarose bioinks incorporating iron oxide MNPs and encapsulating chondrocytes were used to fabricate constructs with random-to-aligned collagen fiber organization recreating the architecture of cartilage.[22]

However, a main limitation of existing extrusion-based magnetically-assisted 3D bioprinting systems is their low potential to control the 3D organization of magnetic elements incorporated within low-viscous bioink during layer-by-layer printing while preserving the design freedom of fabricated constructs. The use of support baths with adequate rheological behavior might enable the magnetically-assisted printing of high-resolution anisotropic constructs. By providing a semi-solid medium with shear-thinning and self-healing properties to print into, the magnetic bioinks can remain viscous long enough after printing to allow the magnetic fields orientate the magnetically-responsive fillers without compromising the resolution of fabricated structures. Granular hydrogels, especially those based on agarose microparticles,[31–33] have been widely proposed as support materials for embedded 3D printing, but the typical polydispersity associated with microparticles suspensions with large sizes resulted in the fabrication of constructs with poor resolution.[34] In this way, the use of nanoparticulated support baths, characterized by higher homogeneity than their microparticulated counterparts, constitutes a better approach to design high-resolution 3D printed constructs. Among them, cellulose nanocrystals (CNCs) suspensions, whose rheological properties can be easily tuned by inducing their partial ion-mediated self-assembly to form shear-thinning gels at low particle concentrations, are especially appealing for maintaining the shape fidelity of the printed composites[35] while allowing the magnetically-induced arrangement of the responsive fillers. Moreover, this kind of support baths also allows the locking of the printed structures within a stable biomimetic fibrillar matrix for their further long-term maturation through the addition of an excess of biocompatible Ca^{2+} ions.[35]

Here, we propose the combination of magnetically- and matrix-assisted 3D bioprinting strategies to engineer high-resolution hybrid composites that are not only able to replicate native tissues anisotropy, but also to provide the possibility for remote actuation during tissue construct maturation. For such purpose, bioinks composed of gelatin-methacryloyl (GelMA), short magnetically-responsive microfibers (sMRFs) and human adipose-derived stem cells (hASCs) were extruded into fibrillar CNCs-based baths under the application of low-strength magnetic fields, thus obtaining high-resolution constructs with controlled anisotropic architectures. The general biological performance of the 3D bioprinted composites and the efficiency of sMRFs as 3D cell contact guidance elements in tissue engineered constructs was demonstrated (**Figure 1**). To test the potential of the proposed concept on a specific anisotropic tissue engineering (TE) application, sMRFs containing tendon decellularized ECM were produced and magnetically-aligned within 3D bioprinted constructs. The synergy between the biophysical and biochemical cues of this biomimetic microstructure, combined with its magneto-mechanical stimulation during in vitro maturation, was shown to boost hASCs mechanosignaling and to promote their commitment toward tenogenic lineage.
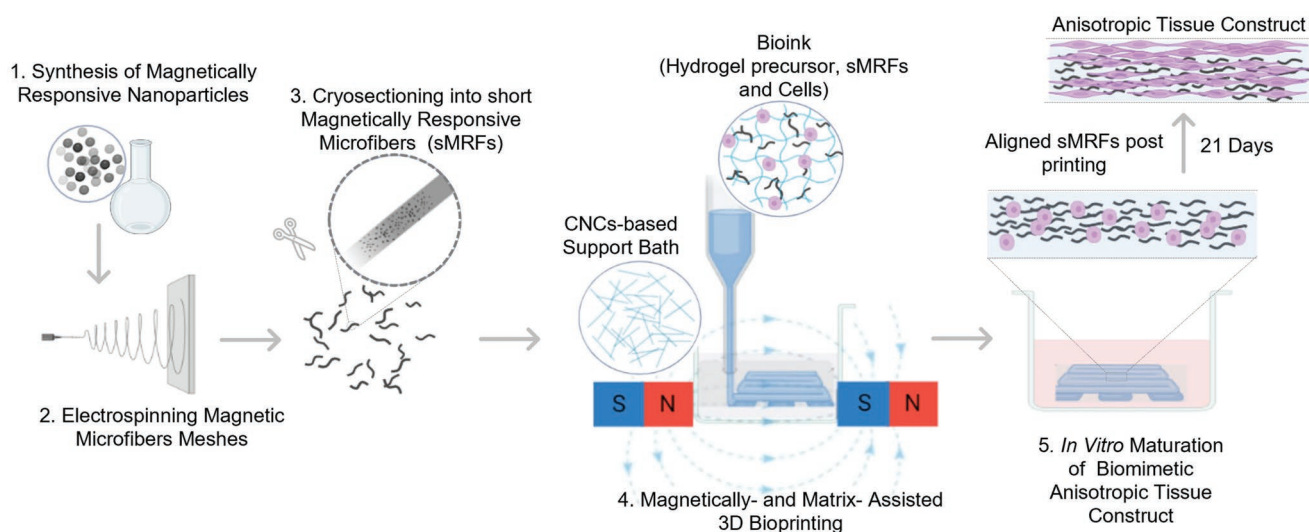
Figure 1. Schematic illustration of the proposed strategy to fabricate high-resolution anisotropic biomimetic constructs: highly-responsive magnetic nanoparticles were synthesized and incorporated in the structure of electrospun microfibers, which were subsequently cryosectioned obtaining short magnetically-responsive microfibers (sMRFs). sMRFs were incorporated together with hASCs in GelMA-based bioink and magnetically-assisted 3D bioprinted embedded in CNCs-based baths to obtain high-resolution constructs with uniaxial anisotropy derived from the alignment of the sMRFs. The designed composites were in vitro maturated under magneto-mechanical stimulation, promoting the proliferation, elongated growth and differentiation of the encapsulated cells.

2. Results and Discussion

2.1. Design and Characterization of Highly-Responsive MNPs: Influence of Synthetic Conditions

MNPs were prepared by synthetic processes based on the thermal decomposition of metallic precursors in the presence of reducing and stabilizing/surfactant agents.[36] By manipulating the ratio between these compounds and/or the synthetic parameters, like reaction temperature or heating rate, MNPs with different physicochemical characteristics can be designed. It is well-known that thermal decomposition is a suitable method to produce MNPs with extremely-high crystallinity and monodispersity, although the obtained particles exhibit hydrophobic behavior, which is a critical drawback for many of their potential biomedical applications.[36,37] However, for the fabrication strategy proposed in this work, the hydrophobicity of the designed MNPs can be exploited for their easy redispersion in the chloroform-based solutions used to prepare electrospun magnetic microfibers.

After the typical thermal decomposition synthesis (see description in the Experimental Section), highly-monodisperse iron oxide MNPs with well-defined spherical morphology and mean core diameter of 9.1 ± 0.9 nm were obtained (**Figure 2**A; see also Figure S1, Supporting Information). The crystalline structure of the MNPs was determined by X-ray diffraction (XRD), obtaining a diffraction pattern that establishes magnetite as the most common iron oxide phase present in the sample (*Fd-3m* symmetry, space group 227) (Figure 2B). The co-existence of parts with maghemite-type organization would also be possible, but the absence of the minor peaks characteristic of this crystallographic structure in the XRD spectrum indicates magnetite as the clearly predominant phase.[38] In order to modify the physicochemical properties of the MNPs and obtain

nanosystems with higher magnetic response (large magnetization values), two different design strategies were evaluated: i) the synthesis of iron oxide MNPs with larger dimensions within the superparamagnetic regime[39] and ii) the doping of iron oxide MNPs with zinc cations.[36] To prepare MNPs with a larger size, the effect of decreasing the concentration of iron (III) acetylacetonate in the precursor solution was evaluated. The obtained MNPs showed a larger diameter (13.2 ± 1.0 nm), maintaining a well-defined spherical shape and a high monodispersity degree (Figure S2, Supporting Information). On the other hand, zinc-doped iron oxide MNPs were prepared by the partial substitution of iron (III) by zinc (II) acetylacetonate in the precursor solution. These zinc-doped iron oxide MNPs preserved the spherical shape and an average diameter of 8.9 ± 0.8 nm (Figure S2, Supporting Information). Moreover, inductively coupled plasma mass spectrometry (ICP-MS) measurements confirmed the incorporation of zinc in the crystalline structure of the MNPs, with a stoichiometric composition of $Zn_{0.28}Fe_{2.72}O_4$ (Table S1, Supporting Information).

The magnetic characterization of the synthesized MNPs showed that zinc doping is a more efficient strategy to improve the magnetic response of the particles than increasing their size (Figure S3 and Table S2, Supporting Information). Iron oxide MNPs with an average diameter of 9.1 ± 0.9 nm displayed a superparamagnetic behavior at 310 K (remanent magnetizations and coercive fields close to zero, that is, hysteresis loop with negligible area), reaching a saturation magnetization value of 66.1 ± 2.8 emu g^{-1}. In the case of 13.2 ± 1.0 nm iron oxide MNPs, magnetometry measurements showed a slight variation on the saturation magnetization value, increasing up to 67.6 ± 2.7 emu g^{-1}. On the other hand, the designed zinc-doped MNPs with 8.9 ± 0.8 nm size displayed a saturation magnetization value of 76.1 ± 3.0 emu g^{-1}, which represents a remarkable increase over iron oxide MNPs without zinc doping of the same

ADVANCED
SCIENCE NEWS
www.advancedsciencenews.com

ADVANCED
FUNCTIONAL
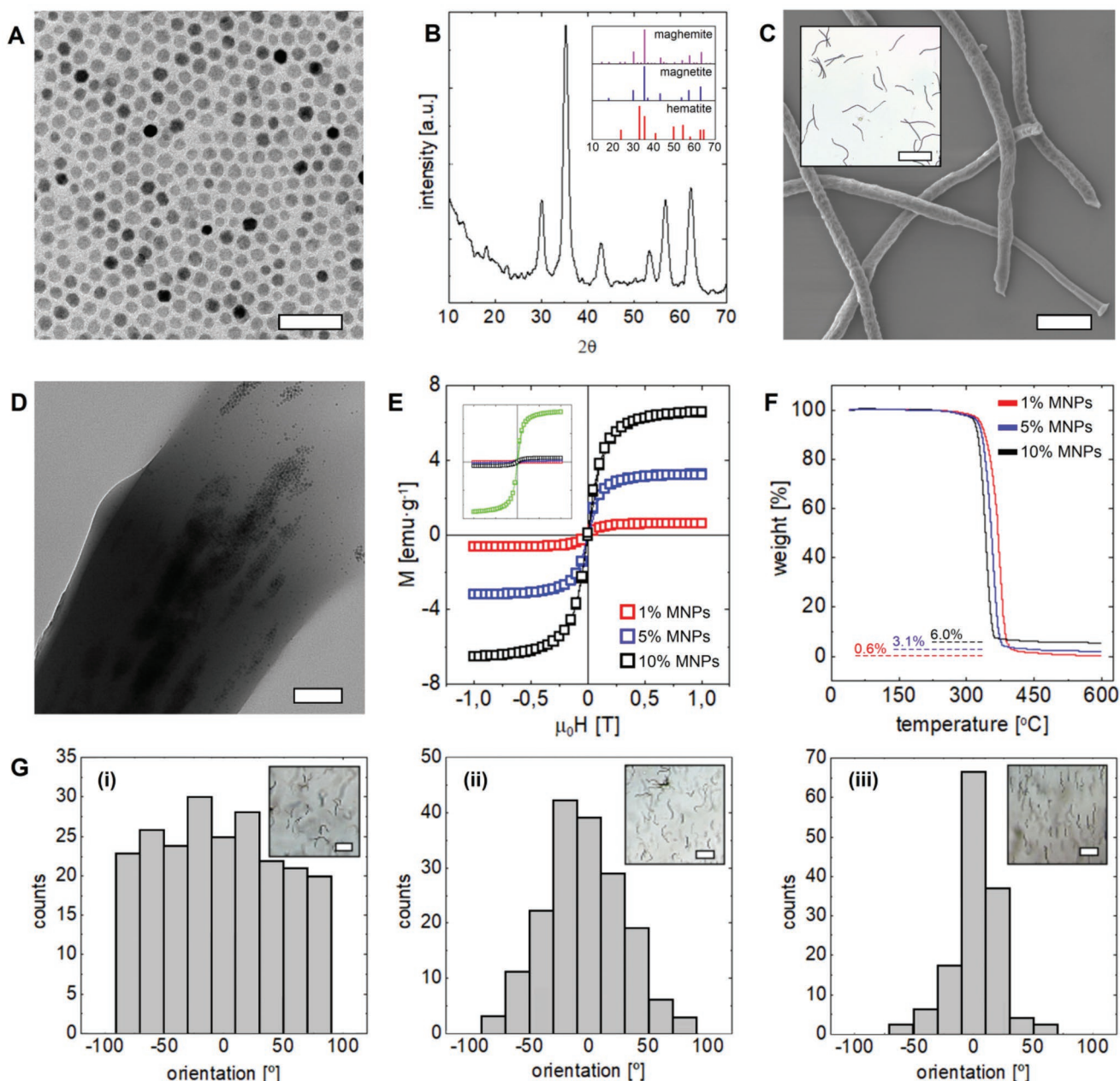**MATERIALS**
www.afm-journal.de

Figure 2. A) TEM image (scale bar 50 nm) and B) XRD spectra of 9.1 ± 0.9 nm iron oxide MNPs. Inset in B) represents the angle positions and relative intensities of XRD peaks for the three main crystalline forms of iron oxide. C) SEM image of sMRFs with 41 ± 11 μm in length (scale bar 5 μm). Inset in C) shows the 4X optical microscopy image of these microfibers (scale bar 100 μm). D) TEM image of a PCL-based sMRFs incorporating 5% (w/w) MNPs (scale bar 100 nm). E) Magnetic hysteresis loops at 310 K of sMRFs incorporating 1% (red), 5% (blue) and 10% (w/w) (black) MNPs. Inset in E) compares the magnetic hysteresis loops of pure MNPs (green) and hybrid microfibers. F) TGA plots of sMRFs containing 1% (red), 5% (blue) and 10% (w/w) (black) MNPs. G) Orientation statistical distributions of 69 ± 17 μm sMRFs modified with 5% (w/w) MNPs within GelMA hydrogels under i) no applied magnetic stimuli, ii) 14 ± 2 mT and iii) 26 ± 3 mT applied magnetostatic fields. Insets show 4X magnification optical microscopy images of the sMRFs within the hydrogels under the different applied magnetic fields (scale bars 500 μm).

size (15.1%). As expected considering their small dimensions, in both cases the designed MNPs also presented superparamagnetic behavior at 310 K.[40] These saturation magnetization values are among the highest reported to date for iron oxide-based MNPs with superparamagnetic behavior at the analyzed temperature.[16,41,42]

The higher magnetic power of larger MNPs is attributed to the lower percentage of atoms placed close to the particle's surface, whose contribution to the magnetization is lower than that of those located in the innermost parts of magnetic nanostructures due to border effects (spin canting).[39,43] Conversely, the increase on the magnetization caused by the doping strategy

is attributed to the distribution of zinc cations in the particle's structure. The spinel crystalline structure of magnetite MNPs consists in Fe^{2+} and Fe^{3+} atoms located in two different positions depending on their coordination with the oxygen atoms: octahedral and tetrahedral positions. The unit cell of magnetite structure has 8 and 16 iron cations in tetrahedral and octahedral positions, respectively, so the structure can be noted as $(Fe^{3+})^{tet}(Fe^{2+}Fe^{3+})^{oct}O_4$. The atomic magnetic moments of tetrahedral and octahedral Fe^{3+} cancel each other, being the magnetization generated only by octahedral Fe^{2+} atoms (ferrimagnetic order). When a certain amount of Zn^{2+} cations are incorporated in the crystalline structure of magnetite-type MNPs, they replace part of the Fe^{3+} cations located in tetrahedral positions, breaking the previously described cancelation effect (zinc cations do not have intrinsic magnetic moment). That is, when part of the tetrahedral Fe^{3+} ions are replaced by Zn^{2+} ones, the equivalent part of the octahedral Fe^{3+} no longer suffers the cancellation effect of its magnetic moment, which translates into a positive contribution to the magnetization of MNPs (see schematic Figure S4 in Supporting Information).[36,44]

According to these results, the $Zn_{0.28}Fe_{2.72}O_4$ MNPs with 8.9 ± 0.8 nm were selected for the following experiments. The use of superparamagnetic zinc-doped iron oxide MNPs has been already proposed for other applications in the biomedical field such as magnetic hyperthermia or magnetic resonance imaging,[36,45] but their use in the area of TE has not been evaluated so far. The most typical strategies reported in the literature to increase the magnetic response of iron oxide MNPs are associated with several limitations related to their magnetic response and/or biocompatibility. For instance, and as mentioned before, increasing the size of MNPs is an easy way to improve their magnetization values. However, the dimensions of the designed MNPs must be at least several tens of nanometers in order to reach remarkable improvements, a fact that compromise the superparamagnetic behavior of the particles and that also can lead to their uncontrolled aggregation when applying magnetic stimuli.[40] Similarly, the design of cubic-shaped MNPs has been also proposed to increase their anisotropy degree and then the net magnetization under the application of external magnetic fields, but this strategy just becomes efficient when the MNPs have large dimensions above the superparamagnetic critical size.[37] On the other hand, although cobalt doping has been widely explored to manipulate the magnetic response of iron oxide nanostructures, this approach is limited to rather low doping degrees due to the inherent toxicity of cobalt ions.[46] Thus, the here proposed zinc doping is an attractive alternative for the design of iron oxide-based MNPs with high magnetic response while incorporating a metallic element with very low toxicity[47] and preserving their reduced dimensions within the superparamagnetic regime.

By exploiting the high magnetic susceptibility of the designed zinc-doped MNPs (Figure S5, Supporting Information), bioink with magnetic response at lower MNPs contents can be formulated, also allowing their subsequent remote manipulation using magnetic fields of lower intensity. In this way, we expect to contribute to minimize the potential toxicity/safety risks associated with the use of high concentrations of magnetic materials and the application of intense magnetic radiations for their manipulation.[26,27]

2.2. Physicochemical Characterization of sMRFs as Anisotropic Magnetic Microfillers

One typical way of creating anisotropic microstructures within bulk hydrogels is based on the direct incorporation of MNPs in the precursor solutions of these materials and their subsequent remotely-induced manipulation with magnetic fields before hydrogel crosslinking.[21,48,49] However, because large amounts of inorganic material may be required to enable this concept, it can compromise the biocompatibility of the designed constructs.[26] In this sense, the use of lower amounts of MNPs to modify microfillers with high aspect ratio emerges as an interesting strategy to reach high anisotropy while using lower concentrations of inorganic materials.[23] In our strategy, the previously synthesized zinc-doped MNPs were incorporated at different concentrations (1%, 5%, and 10% (w/w)) into electrospun polycaprolactone (PCL) microfibers to render them magnetically-responsive (Table S3, Supporting Information). Optical microscopy images demonstrated that homogeneous electrospun magnetic PCL meshes with similar microfiber diameter (between 1.5 ± 0.2 and 1.8 ± 0.3 μm) were formed independently of the relative amount of magnetic material added (Figure S6, Supporting Information). These electrospun meshes were then embedded in optimal cutting temperature compound (OCT) blocks and cut using a cryostat microtome in order to prepare magnetically-responsive fibers with lengths in the micrometer-range (Figure 2C). Three different cut thicknesses were tested: 25, 50, and 100 μm, obtaining sMRFs with average lengths of 41 ± 11, 69 ± 17, and 109 ± 27 μm, respectively (Figure S7, Supporting Information).

TEM characterization and magnetometry measurements were performed to evaluate the incorporation of MNPs in the structure of the sMRFs and their effect over the magnetic behavior of the hybrid constructs. As can be observed in Figure 2D, the MNPs were successfully incorporated within the structure of sMRFs. Moreover, the sMRFs showed magnetic responses proportional to the amount of magnetic material used to prepare hybrid systems (Figure 2E). Thus, the sMRFs with 1%, 5% and 10% (w/w) of MNPs displayed saturation magnetizations of 0.7 ± 0.1, 3.5 ± 0.2, and 6.8 ± 0.3 emu g^{-1}, respectively, with similar superparamagnetic behavior compared to that observed for pure MNPs in all cases (Figure 2E and Table S4, Supporting Information). The compositional analysis of the designed sMRFs through ICP-MS measurements and their thermogravimetric (TGA) characterizations confirmed that the amount of magnetic material present in the different sMRFs samples is in agreement with the PCL-MNPs ratios used in the hybrid precursor solutions. In this sense, ICP-MS data demonstrated that the concentrations of iron and zinc observed in a pure MNPs solution decrease in fibers solutions proportionally to the amount of MNPs incorporated in hybrid structures (Table S5, Supporting Information), while TGA analysis showed that the mass fractions of magnetic material in the sMRFs was 0.6%, 3.1% and 6.0% for the formulation with 1%, 5% and 10% (w/w) of MNPs, respectively (Figure 2E). These values are highly-consistent with the amount of MNPs used to prepare the electrospinning suspensions, considering that 27% of the mass of the MNPs is attributed to their original oleic acid/oleylamine coating, which is also calcinated at

high temperatures during TGA measurements (Figure S8, Supporting Information).

2.3. Magnetically-Induced Alignment of sMRFs within Polymeric Hydrogels

Next, the PCL-based sMRFs were incorporated within GelMA hydrogels to evaluate their potential to be remotely aligned to generate anisotropic constructs. A custom-made two parallel magnets system providing magnetostatic field strengths in the range 14–238 mT was used to generate the magnetic stimuli. To optimize the design of the system, 0.50 mg mL^{-1} of sMRFs with different lengths were incorporated within hydrogel precursor solutions and then the effect of magnetic field strength in the alignment of sMRFs was evaluated and compared to control groups (no magnetic stimulation). For instance, the ≈70 µm sMRFs modified with 5% (w/w) MNPs were randomly oriented within GelMA hydrogels in the absence of magnetic stimulus during fabrication (Figure 2G i). Under an applied 14 ± 2 mT magnetostatic field, the sMRFs began to align, with 22% of the analyzed fibers orienting along the magnetic field direction within ±10° (58% in the range of ±30°) (Figure 2G ii). Conversely, when the magnetic field strength was increased to 26 ± 3 mT, the samples showed higher anisotropic organizations, with 49% of the analyzed sMRFs oriented along magnetic field direction within ±10° (94% in the range ±30°) (Figure 2G iii).

As observed from Figure S9 and Table S6 (Supporting Information), the sMRFs with ≈40 and 70 µm in length could be easily aligned by applying weak magnetic fields (14 ± 2 and 26 ± 3 mT, respectively) when the relative amount of MNPs within their structure is larger than 5% (w/w). However, when these sMRFs are modified with only 1% (w/w) of magnetic material, the minimum magnetic strength required to induce their alignment was higher, especially for longer fibers (43 ± 4 and 66 ± 7 mT for ≈ 40 and 70 µm long fibers, respectively). In the case of ≈110 µm sMRFs, although they could still orient along the magnetic field direction, much stronger magnetic fields in the range 126–208 mT were required to overcome their inertia and induce anisotropic organization within GelMA hydrogels, but with a highly-crooked appearance. Although the showed optical microscopy images were acquired around the middle region of the fabricated GelMA-based hydrogels, we corroborated that the high-uniformity of the applied magnetostatic fields allowed a consistent actuation over the entire hydrogels during the fabrication process, being the sMRFs homogeneously distributed and aligned creating the desired anisotropy throughout the systems.

It is well-known that the use of intense magnetic fields implies different safety/security concerns and might also be related with several adverse or unwanted effects over the irradiated cells (e.g., deformation of intracellular structures, change of membrane permeability, redistribution of stresses within cells or movement of ions in solution giving rise to induced electric fields and currents).[50] In this sense, considering that our sMRFs can be manipulated within polymeric hydrogels through the application of weak magnetic fields (14 ± 2 mT), this represents a remarkable design improvement compared to most of reported magnetic strategies to fabricate anisotropic

hydrogels. Previous works also using magnetically-modified fibers/rod-shaped particles to design anisotropic polymeric hydrogels typically required much higher magnetic field strengths to manipulate the magnetic materials. For instance, a 130 mT magnetic field was applied to align poly(ethylene oxide-*stat*-propylene oxide) rod-shaped microgels modified with MNPs within injectable hydrogels.[51] In a similar approach, electrospun microfibers incorporating iron oxide MNPs were organized inside fibrine hydrogels under the application of 100–300 mT external magnetic fields.[23] Rod-shaped particles composed by cellulose[24] or calcium sulfate[52] and decorated with MNPs were also evaluated as magnetically-responsive fillers to generate anisotropic hydrogels, also requiring magnetic irradiations higher than 100 mT to align them in the direction of the applied stimulus.

Thus, based on our aimed design criteria of minimizing the amount of magnetic material and the required magnetic field strength to create the desired anisotropic patterns, sMRFs with 40 µm in length incorporating 5% (w/w) MNPs that can be aligned with 14 ± 2 mT magnetostatic fields were selected for the further experiments. Moreover, the use of sMRFs with shorter lengths within the analyzed range is also the best choice from a biomimetic point of view. It has been shown that collagen gel fibers in natural ECMs display variable lengths ranging from a few micrometers to a few tens of micrometers.[53,54] In this way, the incorporation of sMRFs with 40 µm in length in the designed hydrogels, instead of the other developed alternatives with longer dimensions, will contribute not only to enhance the magnetic performance of the systems, but also to more-realistically mimic the fibrillar structure of native tissues.

2.4. Optimization of Magnetically-Assisted 3D Printing Processes for the Design of High-Resolution Anisotropic Composites

The previously synthesized sMRFs were incorporated into hydrogel precursor solutions and combined with magnetically-assisted 3D printing strategies aiming to design high-resolution anisotropic multilayer constructs. First, we performed the rheological characterization of GelMA-based solutions, observing that the incorporation of sMRFs has a reduced effect over their viscoelastic properties. In general, all formulations are low viscosity non-Newtonian fluid with shear-thinning properties, which allow their use as inks in extrusion-based 3D printing processes (Figure S10, Supporting Information). In order to orientate the incorporated sMRFs, magnetically-responsive GelMA-based hydrogel formulations were extruded under the presence of external magnetostatic fields created by two parallel neodymium magnets at a distance of 5.1 cm and placed in a custom-made holder (Figure S11, Supporting Information) that can be easily installed on the printing stage (**Figure 3**A). A computational simulation was performed to evaluate the uniformity of the resulting magnetostatic fields, an essential characteristic in order to prevent the accumulation/aggregation of the sMRFs in the regions where more intense field strengths are generated and to induce their uniform alignment/distribution within the 3D printed hydrogels. As it can be observed in the computational simulation (Figure 3B), a region of ≈1.5 cm wide between
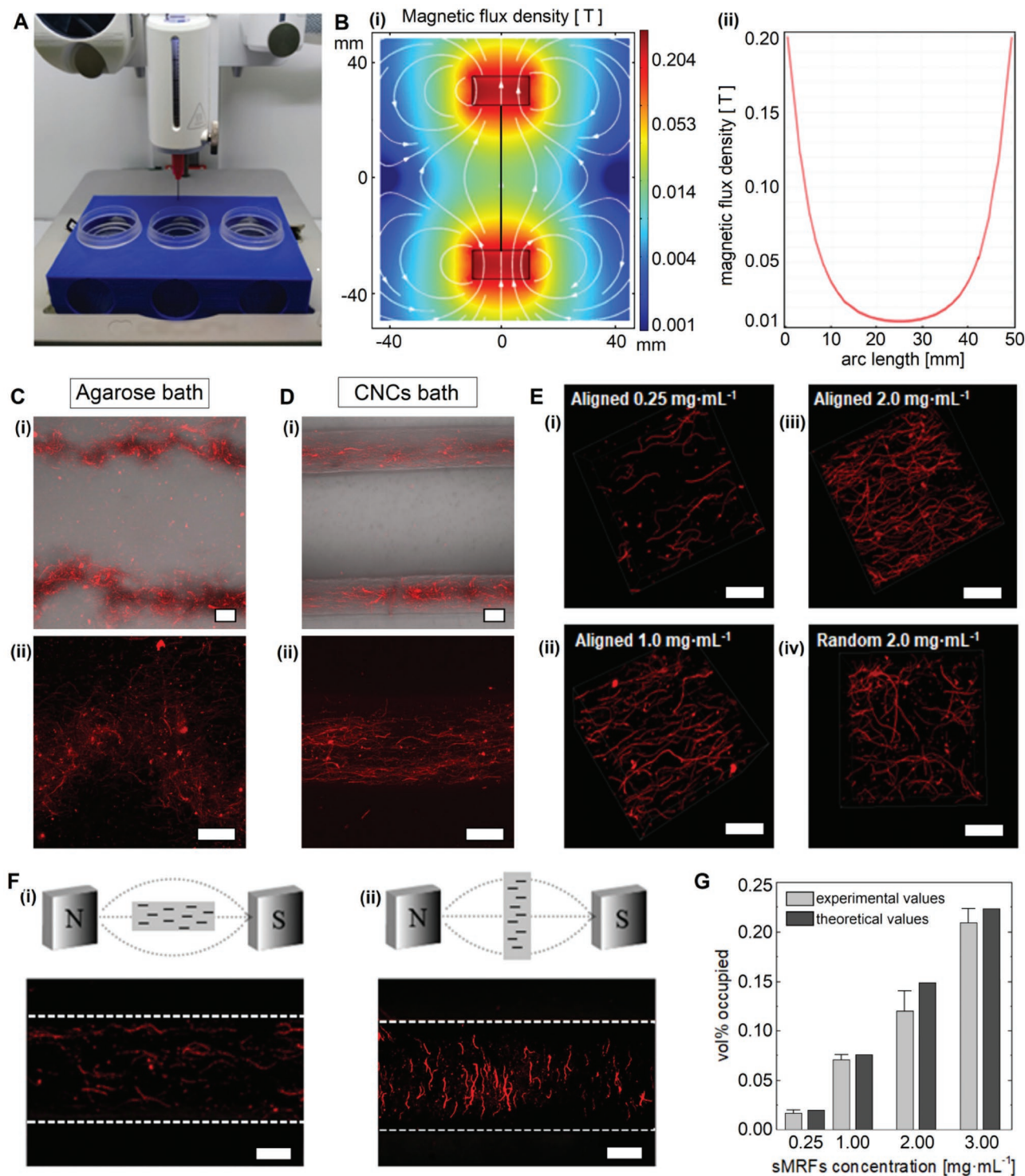
Figure 3. A) Image of magnetically-assisted 3D printing setup, using a custom-made holder that allows the simultaneous arrangement of three pairs of parallel magnets. B) Computational simulations of the magnetostatic field created on the printing surface; i) color map of magnetic flux density in the 2D plane connecting the centers of two parallel neodymium magnets (horizontal plane z = 1.05 cm; magnets height = 2.10 cm) and ii) simulation of the magnetic flux density along the 1D line between the centers of two neodymium magnets. Confocal laser microscopy (CLM) images of GelMA hydrogels loaded with 2.00 mg mL^{-1} sMRFs 3D printed into C) agarose and D) CNCs-based support baths (scales bars 100 μm). E) 3D reconstruction from CLM images of a 100×100×50 μm^3 portion of hydrogel printed into CNC-based support baths with i) 0.25 mg mL^{-1}, ii) 1.00 mg mL^{-1}, and iii) 2.00 mg mL^{-1} of aligned sMRFs and iv) 2.00 mg mL^{-1} of randomly-oriented sMRFs (scales bars 50 μm). F) CLM images of hydrogels printed into CNC-based support baths loaded with 2.00 mg mL^{-1} sMRFs aligned i) parallel and ii) perpendicular to the long direction of the printed filaments (scales bars 100 μm). The sMRFs were stained with rhodamine B isothiocyanate for CLM images. G) Comparison between theoretical and experimental values of the volume occupied by sMRFs in 3D printed hydrogels depending on the incorporated concentration.

the magnets showed a fairly constant magnetic field intensity in the range 14–19 mT, results that were also confirmed by experimental measurements using a gaussmeter (13.9 ± 1.8 mT in the central point between the magnets; and 19.0 ± 2.4 mT at 0.75 cm away from this point along the line defined by the centers of parallel magnets, respectively).

After confirming the uniformity of the magnetostatic field generated on the printing space, we evaluated the performance of two different types of support baths on the matrix-assisted printing process. As previously mentioned, these support baths[55] are required to maintain the shape fidelity and resolution of the printed multilayered constructs when using inks that must remain as low-viscosity liquids for long enough after printing before induce their solidification in order to allow the magnetic orientation of the sMRFs. In this work, agarose microparticles, one of the most commonly used granular materials for embedded printing,[31,32,56,57] and CNCs-based support baths[35] were tested. As observed in Figure 3C, GelMA hydrogels loaded with sMRFs printed in the agarose-based bath led to irregular and tortuous printed filaments with variable diameters ranging from 200 to 650 μm (average diameter 428 ± 110 μm; see Figure S12, Supporting Information). Moreover, although printing was performed under the application of the external magnetostatic stimulus, the sMRFs incorporated in the hydrogels were poorly aligned, diffused out of the printing path and formed large aggregates (Figure 3C). Hence, although embedded printing is essential to achieve the objective of fabricating multilayered high-resolution anisotropic constructs, microparticle-based support baths seem to not meet the requirements to enable this fabrication strategy.

In order to improve the alignment, resolution and fidelity of the designed magnetic composites, we evaluated the use of our previously developed CNCs-based fluid gel to assist the printing process.[35] This fluid gel can be easily prepared by partially screening the surface charge of CNCs with the controlled addition of bivalent calcium ions, leading to a shear-thinning and self-healing material with outstanding performance as support media for matrix-assisted printing. Besides the smoother footprints left by this colloidal fluid gel on printed lines when compared to granular agarose-based gels, this bath also recovers fast from predominantly viscous to predominantly elastic states after the disturbance caused by external mechanical forces, demonstrating its high self-healing potential, an essential characteristic to provide and maintain the high resolution of 3D printed constructs.[35] As shown in Figure 3D, when applying the same printing parameters used to print in agarose baths, the magnetic inks printed in the CNCs fluid gels resulted in well-defined and straight filaments. In this support bath, the printed filaments presented a consistent diameter of 226 ± 34 μm, being comparatively better defined and more uniform than those printed in agarose and with the incorporated sMRFs well-confined within the limits of the printing path (Figure S12, Supporting Information). Together, these set of physical and rheological properties of CNCs fluid gels allowed the adequate alignment of sMRFs incorporated in the ink filaments upon application of a magnetic field during the printing process. Thus, the 14 ± 2 mT magnetostatic field created on the printing space could induce the uniform distribution and uniaxial alignment of the sMRFs along the main axis of the filaments, creating the desired anisotropic microstructure in the printed hydrogels constructs.

After demonstrating the importance of the CNCs-based support bath to enable the proposed magnetically-assisted 3D printing concept, we next evaluated the effect of the concentration of sMRFs (between 0.02 and 3.00 mg mL^{-1}) in GelMA inks over the microstructure of the 3D printed constructs. At the lowest analyzed concentration, sMRFs were aligned and uniformly distributed in the hydrogels with an average microfibers interdistance of 79 ± 16 μm (perpendicular to the applied magnetic field) in the same 2D plane. As expected, the spacing between the aligned sMRFs decreased when the amount of hybrid microfillers increased, observing a minimum interdistance of 9 ± 3 μm when the concentration of sMRFs in the inks was 3.00 mg mL^{-1} (Figure S13, Supporting Information). Although small microfibers aggregates could be observed at concentrations higher than 0.75 mg mL^{-1}, this undesirable phenomenon was only relevant when the concentration of sMRFs was larger than 2.00 mg mL^{-1} (Figure 3E; see also Figures S13 and S14, Supporting Information). This aggregation is attributed to the magnetic dipolar attraction between the sMRFs and their physical entanglement, being both phenomena more relevant when the interdistance between the sMRFs decreases.

To better illustrate the effect of the applied magnetic field over the arrangement of the sMRFs within the hydrogels printed in CNCs-based baths, we printed constructs in the absence and presence of magnetic field (Figure 3E iii-iv), the latter applied parallel (as in previous experiments) but also perpendicular to the direction of the printed filaments (Figure 3F i-ii). In all cases, the CNCs fluid gel allowed the fabrication of high-shape fidelity structures, showing sMRFs aligned parallelly (Figure 3F i) or perpendicularly (Figure 3F ii) to the printed filament, depending on the configuration of the magnetic field, in contrast to the random distribution of sMRFs in the absence of applied magnetic field (Figure 3E iv). These results confirm that the alignment of the sMRFs is exclusively attributed to their magnetically-responsive properties, and not to other phenomena related to the shear stress applied on the inks during the extrusion printing. This fact supposes a remarkable advantage of the proposed concept compared to other fabrication strategies that rely on shear stress to create anisotropic structures using fibrous hydrogel bioinks, thus not being possible to control the fibers alignment direction within the printed constructs.[53,58] The low effect of the shear stress applied during the extrusion by itself over the alignment of the sMRFs is in good agreement with previous works.[58] Thus, it has been demonstrated that shear forces created by extruding the composite inks through a needle are efficient to orient short electrospun microfibers with lengths below 20 μm, but the alignment degree is lower when using longer microfibers and at the volume fraction we applied here.[58]

Afterward, we determined the fraction volume occupied by the hybrid microfillers in the printed structures. 3D printed hydrogels loaded with 0.25, 1.00, 2.00, and 3.00 mg mL^{-1} of aligned magnetic microfibers were analyzed. The 3D reconstructions of confocal fluorescence images of the printed structures showed that the relative volume occupied by the sMRFs

was highly-consistent with the expected values derived from theoretical calculations (see Figure 3G and Calculation S1 in Supporting Information). Thus, we showed that the sMRFs were successfully incorporated and homogeneously distributed within the 3D printed hydrogels, demonstrating that the metallic printing nozzles do not retain them by magnetic attraction during the fabrication process, as well as the homogeneity of the applied magnetostatic fields.

Finally, before incorporating cells in our systems, we prepared neat GelMA and hybrid GelMA-sMRFs cylindrical hydrogel blocks and evaluated their viscoelastic behavior. As expected, it was oberved that the incorporation of stiff hybrid sMRFs leads to an increase in the viscoelastic properties of GelMA-based constructs, being this effect more evident at higher microfillers concentrations.[23,24] On the other hand, by comparing the composite hydrogels loaded with aligned and randomly-oriented sMRFs, it was determined that the latter group displayed higher storage moduli, which was attributed to the larger degree of fiber's entanglement occuring when they have no preferential orientation within the polymeric networks (Figure S15, Supporting Information).[23] The stiffness profiles of the designed GelMA-based hydrogels is consistent with previously reported data for similar composite systems.[23,24,59]

Based on the obtained results, 2.00 mg mL^{-1} sMRFs load was chosen for further experiments, since it showed the best distribution in the 3D printed hydrogels without remarkable aggregation. As mentioned before, MNPs have potential toxicity concerns associated to their use in biomedical applications, which are highly-dependent not only on their physicochemical properties, but mainly on the used concentrations.[26] The amount of magnetic material in our 3D printed hydrogels (with 2.00 mg mL^{-1} of sMRFs modified with 5% (w/w) MNPs) is ≈0.07 mg mL^{-1}, which corresponds to a volume occupation of 0.0011% (v/v) (see Calculation S2 in Supporting Information). This low value, together with the weak magnetic field strengths used to fabricate the anisotropic hydrogels, demonstrates the excellent performance of our system to minimize the toxicity/safety risks derived from high MNPs concentrations and large magnetic field intensities. The use of magnetically-modified sMRFs allowed a significant decrease in the amount of magnetic material required to generate the desired anisotropic structures, compared to 3–5 mg mL^{-1} MNPs typically required to form strings consisting entirely of magnetic material within hydrogels.[21,60] On the other hand, the design of highly-responsive MNPs that we propose here allowed to reduce the overall amount of magnetic material in the hydrogels when compared with most studies using magnetically-responsive elongated microfillers. Thus, we found that relatively high amounts of MNPs (up to 10% (w/w)) are typically required to provide the microfillers with magnetic behavior in order to induce their remote alignment and reach the desired anisotropy degree.[23,61,62] Furthermore, large concentrations of magnetic microfillers, ≈1.5%–3.0% (v/v), are commonly incorporated in the hydrogels,[51,62] resulting in composites with much larger presence of magnetic material than the ones developed here (0.14% (v/v) in our system; see Calculations S1 and S2 in Supporting Information).

2.5. sMRFs Alignment Dictates Cell Spreading and Organization in 3D Bioprinted Constructs

To investigate whether the topographical cues provided by the sMRFs are effective to guide cell spreading and alignment along direction of microfibers orientation, we encapsulated hASCs in our magnetically-responsive hydrogel precursor solutions (i.e., GelMA 7.5% (w/v) and sMRFs) to formulate magnetic bioinks. hASCs were selected as representative cell source due to their potential differentiation into multiple lineages along with their wide availability and extended use for TE purposes.[63]

First, we evaluated the effect of sMRFs orientation and concentration over the alignment and morphology of the encapsulated hASCs (**Figure 4**A). Based on the previous optimization process, sMRFs concentrations up to a maximum of 2 mg mL^{-1} were analyzed in order to avoid fibers entanglement/aggregation within the GelMA-based hydrogels. As expected, when the hybrid composites were loaded with 2 mg mL^{-1} of non-aligned sMRFs (fabricated in the absence of applied magnetic field), the encapsulated hASCs did not show any preferential orientation after 7 days in culture, confirming that shear stress solely is insufficient to induce anisotropic cell organizations. A similar cell behavior was observed in anisotropic hydrogels designed with low concentrations of aligned sMRFs (0.25 mg mL^{-1}). An increment on the percentage of cells arranged in the direction dictated by hydrogel anisotropy was observed when the concentration of magnetically-aligned sMRFs was increased to 1.00 mg mL^{-1}, although a portion of hASCs were still oriented in other directions. However, when the concentration of sMRFs was increased to 2.00 mg mL^{-1}, the dense anisotropic topography of the 3D constructs induced the alignment of a higher number of cells (Figure 4D). The content of sMRFs within the hydrogels also had a remarkable impact on cell morphology. Although hASCs showed a typical spindle shape in all hydrogels, their aspect ratios tend to increase with the increasing of sMRFs concentration, and was markedly higher for cells encapsulated in the designed hydrogels loaded with 2.00 mg mL^{-1} sMRFs after 7 days in culture (Figure 4A; see also Figure S16, Supporting Information). In the high-magnification confocal microscopy images, it can be observed that encapsulated cells adhered to the surface of the aligned sMRFs and followed fiber orientation (Figure 4B). This phenomenon is more relevant when the interspace between successive aligned sMRFs (depending on fibers concentration, see Figures S13 and S14, Supporting Information) decreases, which increases anisotropic cellular organization within the printed constructs. In this way, we can attribute the high orientation degree of hASCs in the hydrogels loaded with 2 mg mL^{-1} of aligned sMRFs to the high contact guidance phenomena between cells and densely packed fibers (interdistance 9 ± 3 μm). However, at the lowest analyzed concentrations of aligned sMRFs, the large interspace between successive fibers (51 ± 11 μm) minimized the contact between them and cells, allowing the almost free spreading of the hASCs and the establishment of randomly oriented cell-cell connections. Thus, we established that uniaxially aligned sMRFs at 2.00 mg mL^{-1} concentration had the strongest effect on inducing the anisotropic growth and orientation of the encapsulated hASCs within the hybrid composites, being this the concentration selected for further magnetically-assisted 3D bioprinting experiments.
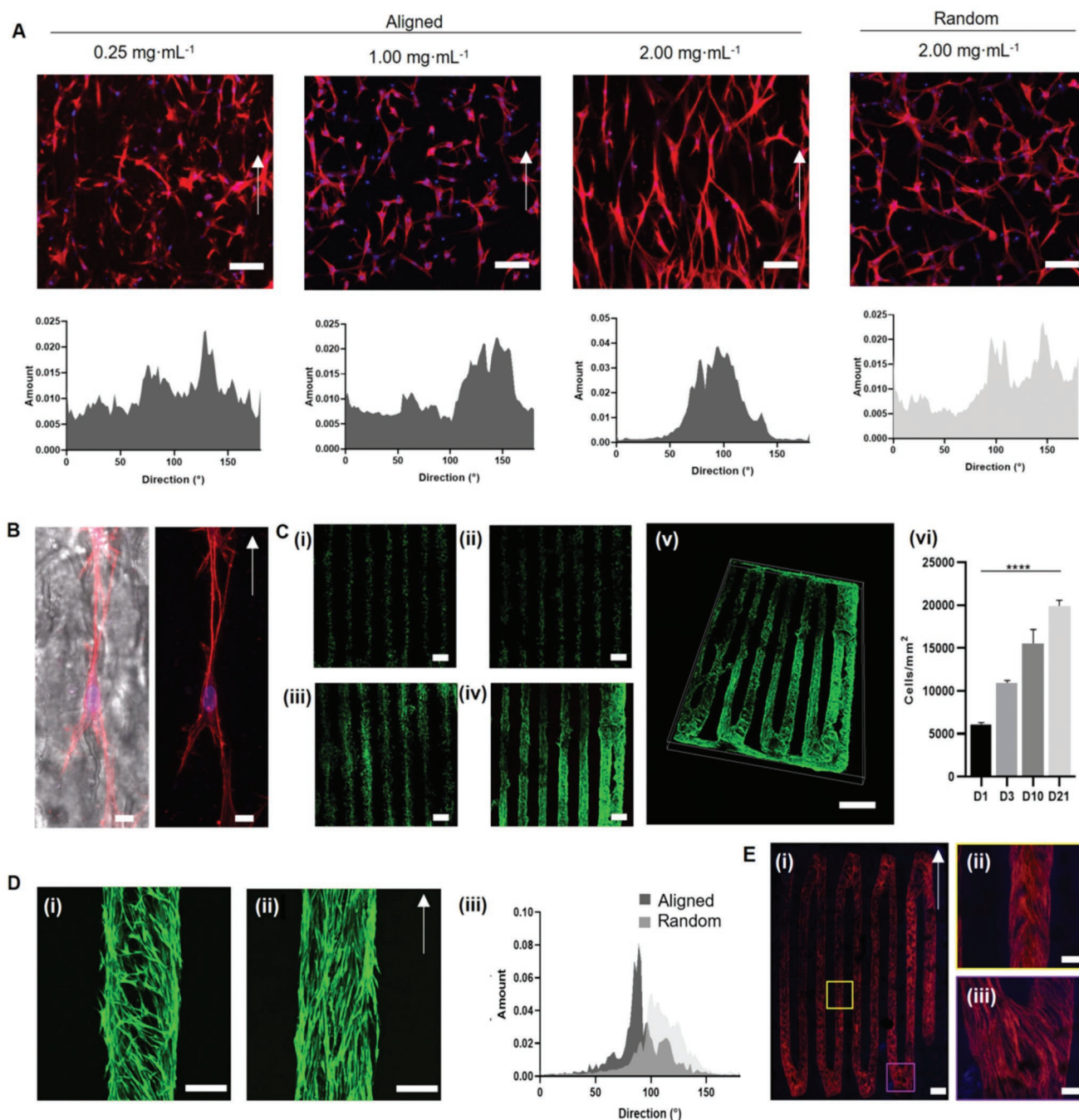
Figure 4. A) CLM images of F-actin staining hASCs encapsulated in GelMA hydrogels with variable concentration of sMRFs (0.25, 1.00 and 2.00 mg mL^{-1} of aligned fibers, and 2.00 mg mL^{-1} of random fibers) after 7 days in culture (Scale bars 75 μm; white arrows indicate the direction of the applied magnetic field during fabrication), along with their orientation plots. B) CLM images of hASCs adhered to sMRFs and acquiring elongated morphologies in 3D bioprinted GelMA hydrogels loaded with 2.00 mg mL^{-1} sMRFs (Scale bars: 10 μm). C) Viability and orientation of the hASCs encapsulated within GelMA-based 3D bioprinted constructs after i) day 1, ii) day 3, iii) day 10 and iv) day 21 of cell culture (Scale bars 750 μm). v) Day 21 tile scan of anisotropic construct (Scale bar 2000 μm). vi) Estimation of cell proliferation based on cell density by construct areas over a culture period of 21 days (****$p < 0.0001$ determined by one-way ANOVA followed by Bartlett's test). D) Cell viability after 21 days in 3D bioprinted hydrogels with 2.00 mg mL^{-1} of i) randomly-oriented sMRFs and ii) aligned sMRFs (Scale bars 250 μm). iii) Plot of cells orientation within the composites with random and aligned sMRFs. E) CLM images of hASCs cytoskeleton in GelMA after 4 weeks in culture stained with F-actin; i) tile scan of fabricated construct, ii) straight line of the printed filaments, iii) curve of the printed filaments (Scale bars: i) 1000 μm, ii,iii) 250 μm).

Cell-laden filamentous constructs with different 3D structures have been bioprinted embedded in the CNCs support baths (see photographs of the finalized prints in Figure S17, Supporting Information), with similar resolution to those observed on the composites fabricated without encapsulated hASCs (Figure S18, Supporting Information). On the other

**ADVANCED
SCIENCE NEWS**

www.advancedsciencenews.com

**ADVANCED
FUNCTIONAL
MATERIALS**

www.afm-journal.de

hand, the cells showed high viability immediately after printing and started to spread and proliferate at longer culture times (Figure 4C; see also Figure S19, Supporting Information). This indicates that neither the printing process nor the use of MNPs or magnetic irradiations had a negative impact on encapsulated cells. After long-term culture (21 days), in both the 3D printed composites fabricated in the absence (random sMRFs) and presence (aligned sMRFs) of magnetic stimulus, the encapsulated hASCs were homogeneously distributed throughout the hydrogels and maintained high viability degrees (Figure 4D). Moreover, we also confirmed that the cells followed the orientation dictated by the incorporated sMRFs even after long culture periods (Figure 4D iii). The shape fidelity of the 3D bioprinted constructs was also well-maintained after 21 days in culture, and cells appear fully confluent as confirmed by the F-actin staining of cytoskeleton. The encapsulated hASCs tend to follow the orientation established by the aligned sMRFs not only in the straight lines of the printed pattern but also in its turns, indicative of the success of the proposed strategy to create anisotropy within the hydrogels (Figure 4E).

2.6. Tendon dECM Microfibers Alignment Directs Adipose Stem Cells Commitment toward Tendon Phenotype

It is well established that the topographical cues derived from the architecture of engineered biomimetic constructs have crucial effects over the spreading, migration and phenotype commitment of the encapsulated cells.[63] To test the potential of our biofabrication concept on a specific tissue engineering challenge, here we have chosen tendon as representative anisotropic tissue and evaluated the functionality of the proposed design to direct hASCs phenotype commitment toward the tenogenic lineage. In addition to the aforementioned impact of biophysical cues stemming from anisotropic organization over cell fate commitment, the biochemical cues derived from the composition of native ECMs also have key roles in this process.[63,64] One interesting way of incorporating these biochemical cues into bioengineered systems is by using decellularized matrix (dECM), alone or blended with other polymers, as scaffolding materials.[65–68] In order to create the adequate niche to provide the encapsulated hASCs with the desired biophysical and biochemical cues for their differentiation toward tendon-lineage, we synthesized hybrid magnetically-responsive electrospun microfibers made not only of PCL and MNPs, but also incorporating a fraction of tendon dECM in their composition (see Experimental section and Table S3, Supporting Information). The obtained PCL-dECM short magnetically-responsive microfibers (dECM-sMRFs) showed dimensions and magnetic properties similar to those of their bare PCL counterparts (Figure S20, Supporting Information).

The bioinks were formulated by incorporating hASCs together with 2 mg mL^{-1} of dECM-sMRFs into GelMA solutions prior to their magnetically-assisted 3D embedded bioprinting in CNCs-based support baths. After the fabrication process, the designed cell-laden composites were continuously magneto-mechanically stimulated during the culture period through the application of 194 ± 13 mT oscillating magnetic fields with 2 Hz oscillation frequency and 0.2 mm displacement (see schematic

flowchart in **Figure 5**A). Although this magneto-mechanical stimulation capability is an inherent feature of hydrogels loaded with magnetically-responsive materials, very few works have explored its potential for providing mechanical stimuli to cells during in vitro maturation process.[20,62,69] Thus, beyond recreating the anisotropy and the specific biochemical cues of native tendon tissues, this strategy allows to provide cells with dynamic mechanical stimuli, which are known to promote the tenogenesis of stem cells and maturation of bioengineered tendon constructs.[70–73]

To test the effectiveness of our system in delivering mechanical stimuli to encapsulated hASCs, we first evaluated the cellular localization of YAP (Yes-associated protein) and TAZ (transcriptional coactivator with PDZ binding motif), two key proteins in the mechanotransduction pathways. YAP/TAZ is predominately cytoplasmic, but upon activation they translocate to the nucleus, where they regulate the expression of different mechanosensitive genes. Their nuclear localization might be triggered by different cellular stimuli, including cytoskeletal tension derived from cell polarization and action of external mechanical forces.[74–76] Immunofluorescence images clearly showed that, although YAP/TAZ were expressed in both static (Figure 5B i) and magnetically-stimulated constructs (Figure 5B ii), a markedly higher nuclear YAP/TAZ localization can be found in the stimulated group (Figure 5B iii). These results indicate that our system is capable to deliver externally generated forces to encapsulated cells and activate YAP/TAZ mechanosignaling, an effect that the fibrillar microstructure of the designed hydrogels alone is not capable of triggering and which will ultimately impact on cells morphology, proliferation and differentiation.[77,78] This is consistent with previous works where YAP/TAZ were identified as key mechanosensing transducers of cell microenvironment mechanical cues, known to play a critical role in determining cell fate.[70,72,78–80]

To analyze the impact of the biophysical and biochemical cues provided by the designed hydrogels and its synergy with the magneto-mechanical stimulation on hASCs differentiation, gene expression analysis and immunofluorescence staining of tendon-related markers were performed. As expected, F-actin staining confirmed that encapsulated cells displayed elongated morphologies and were aligned in the direction dictated by the orientation of the incorporated dECM-sMRFs in both groups (constructs cultured in the presence and absence of magneto-mechanical stimulation).[81,82] In general, most of the tenogenic-related genes analyzed were shown to be upregulated in both groups during time of culture, suggesting that the biophysical and biochemical cues of 3D bioprinted constructs are themselves effective to promote the tenogenic commitment of hASCs. In particular, scleraxis (SCX) and tenomodulin (TNMD), two of the mostly recognized tendon specific markers,[83] showed a consistent pattern of activation dependence, where the earlier SCX upregulation promoted the later upregulated expression of TNMD.[84] Remarkably, although its expression was upregulated in both groups (Figure 5C,D), TNMD expression was significantly higher in the composites magneto-mechanical stimulated during culture period (Figure 5D i). Its expression at protein level was further confirmed by the immunostaining of fabricated constructs after 21 days of culture (Figure 5D ii).
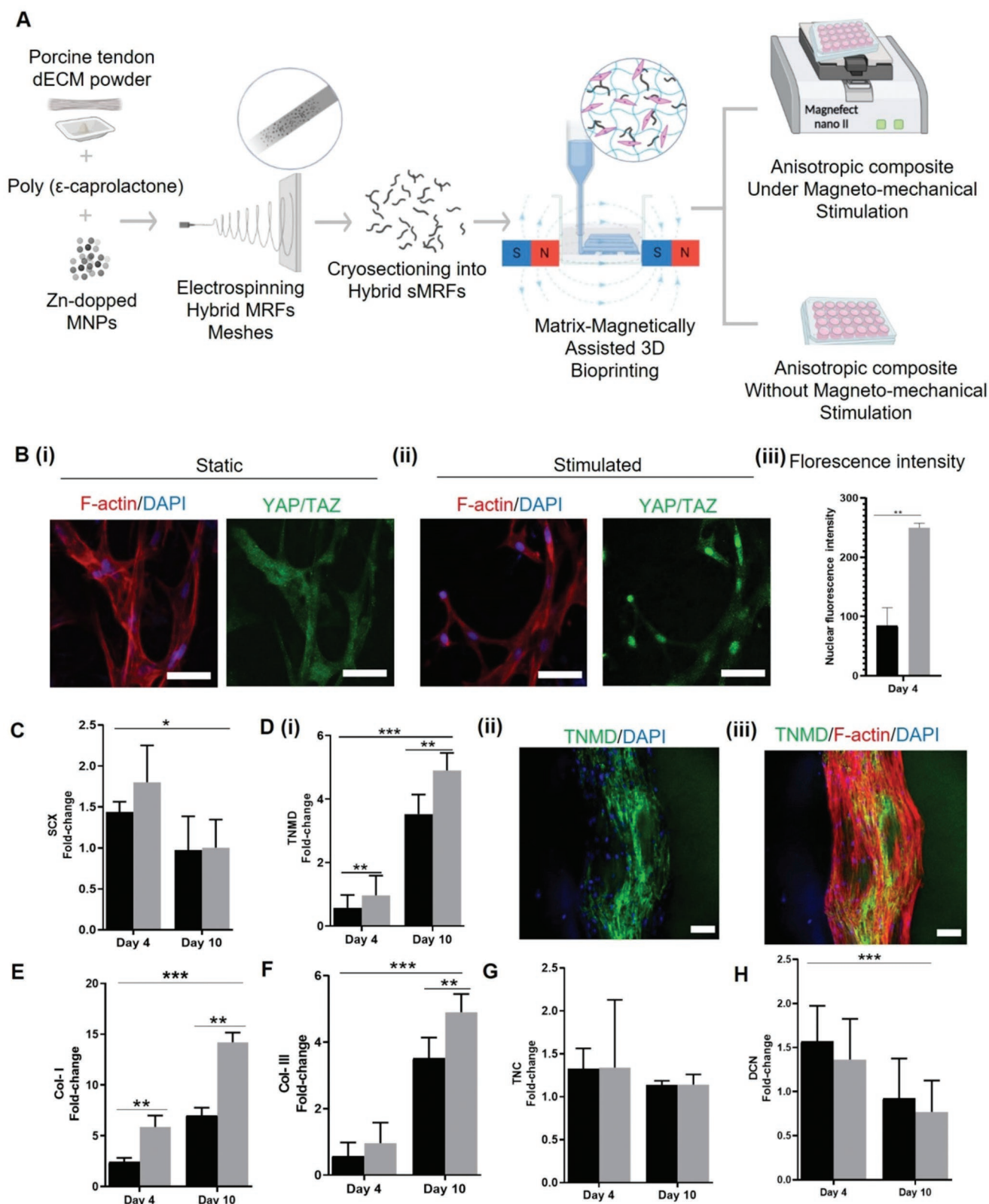
Figure 5. A) Schematic flowchart illustrating experimental design for fabricating dECM-sMRFs followed by magnetically- and matrix-assisted 3D bioprinting of tendon biomimetic composites with and without mechano-magnetic stimulation during maturation process. B) CLM images of 3D bioprinted anisotropic constructs for nuclear translocation of YAP/TAZ antibody with stained cytoskeleton (red), nucleus (blue) and YAP/TAZ (green) on day 4 of cell culture in the i) absence and ii) presence of magneto-mechanical stimulation (hASCs encapsulated in GelMA-based hydrogels with

Interestingly, TNMD is a marker for tendon formation, but is also recognized as a tension-regulating protein whose expression is favored by mechanical stimuli in both tendon tissues and bioengineered constructs,[72,85] justifying its significant upregulation in magneto-mechanically stimulated hydrogels. The cellular effects of magneto-mechanically stimulation were also reflected on the gene expression patterns of two main tendon ECM proteins, namely collagen I (Col I) and collagen III (Col III). Tendons ECM is predominantly composed by Col I, while the remaining part comprises of Col III and proteoglycans.[86] Previous studies in the field have demonstrated that the combination of architectural anisotropy and mechanical stimulation lead to the upregulation of these ECM genes in tissue engineered constructs.[85,87] Similarly, our results also showed significantly higher expression of Col I and Col III genes in constructs maturated under magneto-mechanical stimulation (Figure 5E,F). Overall, these results suggest that the anisotropic microstructure created through the magnetically-induce alignment of the dECM-sMRFs within the 3D bioprinted hydrogels, together with the biochemical cues derived from the incorporation of dECM in microfibers formulation, guided the commitment of hASCs toward the tenogenic phenotype, an effect that was boosted by the remote magneto-mechanical stimulation of the constructs during their maturation process.

The magnetically-responsive system proposed here provides an alternative approach to address some limitations of existing tendon TE strategies based on the use of stem cells-laden hydrogels, namely the generation of adequate 3D microenvironmental cues to guide their morphogenesis and differentiation toward the tenogenic phenotype.[83,88,89] Moreover, it further incorporates the additional functionality of enabling remote mechanical actuation of the constructs during its in vitro maturation, a concept that might be continued in vivo after transplantation to promote better construct engraftment with host tissue and improve its regeneration potential.[90–93] It is worth mentioning that, in our system, hASCs differentiation derives exclusively from the bioinspired biophysical and biochemical cues of 3D constructs and their synergy with the applied magneto-mechanical stimuli, not requiring additional biological factors.[94] This represents a comparative advantage with many other tendon TE strategies, where supplementation with expensive growth factors, such as bone morphogenetic protein 12 (BMP-12) or TGF-β, are required to promote the tenogenesis of stem cells for tendon TE applications.[95–97]

The design principles that we applied here were directed to meet the specific needs of tendon tissues. However, the general concept has broad scope application and could be explored to engineer other tissues with uniaxial anisotropic structures (e.g., skeletal muscle), or even with more complex hierarchical anisotropy (e.g., cartilage, cardiac).

3. Conclusion

In this work, we developed a new fabrication strategy for the design of bioinspired anisotropic composites based on hydrogel bioinks incorporating sMRFs. The high magnetic response of the MNPs incorporated in sMRFs allowed their remote alignment within low viscosity GelMA inks by weak magnetic field strengths (14 ± 2 mT), as well as using low contents of magnetic material to create the desired degrees of anisotropy. The use of support baths based on CNCs fluid gels reveled essential for enabling the layer-by-layer printing of high-resolution constructs with anisotropic sMRFs alignment by the generated magnetostatic fields on the printing stage (matrix- and magnetically-assisted 3D bioprinting). Besides enabling the proposed fabrication processes, the magnetic sMRFs further provided the systems with the additional capability of magneto-mechanical stimulate cells encapsulated in the 3D bioprinted constructs during their culture period. Tendon was chosen as a representative anisotropic tissue to test the biofabrication potential of the proposed concept. For this application, tendon dECM was incorporated in sMRFs to provide bioinks with tissue-specific biochemical cues. Obtained results show that the tendon-mimetic microenvironment derived from the anisotropically aligned dECM-sMRFs induced the tenogenic commitment of hASCs. Remarkably, the magneto-mechanical actuation of the constructs during their maturation process effectively activates cell mechanosignaling and significantly increased the observed tenogenic effects. Overall, we foresee that combining highly-responsive magnetic materials with matrix- and magnetically-assisted 3D bioprinting, while further leveraging on the inherent magneto-mechanical actuation functionality of produced constructs for cell stimulation, represent an attractive biofabrication strategy to engineer anisotropic mechanosensitive tissues.

4. Experimental Section

MNPs Synthesis: Spherical-shaped MNPs were prepared through thermal decomposition processes in a 100 mL three-neck bottom-round flask connected to a Schlenk line and a water reflux condenser, using a heating mantle to control the temperature. Following previously reported procedures, in a typical synthesis of iron oxide MNPs with an average diameter of ≈9 nm, 3 mmol of iron (III) acetylcetonate, 10 mmol of 1,2-hexadecanediol, 6 mmol of oleic acid, 6 mmol of oleylamine and 20 mL of benzyl ether were added to the flask (all reagents purchased from Sigma–Aldrich). Under continuous 700 rpm magnetic stirring, the temperature of the solution was increased to 110 °C and then a 10 mbar vacuum was applied for 1 h. After that, vacuum was exchanged by nitrogen flow using the Schlenk line and the temperature was increased to 210 °C (heating ramp 8 °C min^{-1}) and maintained for 2 h. Finally, the temperature was increased to 295 °C (5 °C min^{-1}) and the solution maintained under reflux for 1 h. After cool down to room temperature,

---

2.00 mg mL^{-1} of dECM-sMRFs) (Scale bars 50 µm), and iii) quantification of fluorescence intensity for YAP/TAZ antibody nuclear translocation in stimulated and static groups on day 4 (**$p < 0.005$ determined by two-tailed Student's t-tests with Welch's correction). Cells expressed higher levels of diverse tenogenic genes when cultured in static and stimulated groups for 4 and 10 days: C) Scleraxis (SCX), D) i) Tenomodulin (TNMD), ii,iii) immune staining for TNMD antibody with stained cytoskeleton (red), nucleus (blue) and TNMD (green) (Scale bars 250 µm), E) type I collagen (COL1A1), F) type III collagen (COL3A1), G) Tenascin-C (TNC), and H) Decorin (DCN) (***$p < 0.0001$, **$p < 0.005$, *$p < 0.05$ determined by two-way ANOVA followed by Tukey's post hoc tests). In the plots in subfigures (B–D), color columns correspond to the samples non-stimulated (in black) and magneto-mechanical stimulated (in grey) during in vitro maturation.

**ADVANCED
SCIENCE NEWS**

www.advancedsciencenews.com

**ADVANCED
FUNCTIONAL
MATERIALS**

www.afm-journal.de

an excess of ethanol was added to the solution before centrifuge at 4000 rpm 10 min. to precipitate the particles.

MNPs with slightly larger diameter (≈13 nm) were prepared by decreasing the amount of benzyl ether used to prepare the precursor solution to 10 mL, while the partial substitution of iron (III) (2.4 mmol) by zinc (II) acetylacetonate (0.6 mmol, Sigma–Aldrich) resulted in iron oxide-based MNPs doped with zinc.

Tendon Extracellular Matrix Decellularization: The decellularization of native porcine Achilles tendons was performed by modifying a previously reported protocol.[98] Briefly, 10 mM Tris-HCL in PBS hypotonic solution was prepared to store dissected native tissue from porcine flexor tendon and frozen at −80 °C. Later, the sample was thawed and hypotonic solution was replaced by 1.5 mM NaCl in 50 mM Tris-HCl hypertonic solution. Then, the samples were shaken in distilled water and frozen again at −80 °C, repeating the freeze-thaw cycle several times. After that, the samples were incubated for half hour in 0.05% Trypsin-EDTA (Sigma–Aldrich) at room temperature and then shaken for 4 days soaked in 2% (w/v) SDS solution in PBS. To ensure samples do not have residual surfactant, they were shaken for additional 7 days in PBS solution. The decellularized samples were ground into powder after being freeze dried at stored at −20 °C until further use.

sMRFs Synthesis: Magnetically-responsive PCL microfibers were prepared by electrospinning processes, being the magnetic behavior provided through the incorporation of previously designed MNPs in the polymeric precursor solutions. In a typical synthesis, PCL (Mn = 80 000, Sigma–Aldrich) was dissolved at 17% (w/v) concentration in a 70/30 (v/v) chloroform/N,N-dimethylformamide (DMF) mixture (from Laborspirit and Fisher Scientific, respectively). Prior to mixing the solvents, MNPs were dissolved in the chloroform phase (1-10% (w/w) respect to PCL), exploiting their high stability in this solvent provided by their hydrophobic oleic acid/oleylamine coating, while rhodamine B isothiocyanate (Sigma–Aldrich) was dissolved in the DMF phase (0.1% (w/w) relative to PCL). A similar procedure was performed to prepare hybrid magnetic PCL-tendon dECM microfibers. In this case, a 70/30 (w/w) mixture of PCL and tendon dECM was solubilized in 1,1,1,3,3,3-Hexafluoro-2-propanol (HFIP, Fluorochem), keeping the global concentration of 17% (w/v) and 5% (w/w) of MNPs. As small amount of chloroform (5% (v/v) relative to HFIP) was used to improve the dispersion of the hydrophobic MNPs.

The solutions were magnetically stirred for 24 h (PCL-MNPs) or 48 h (PCL-dECM-MNPs), loaded in 5 mL syringes and electrospun under different conditions (Table S2, Supporting Information). After that, the electrospun membranes were cut in 3×3 mm portions and embedded in OCT (Sigma-Aldrich) blocks that then were frozen at −20 °C and micro-cut at different thickness using a cryostat microtome. The obtained short microfibers were washed several times with water to remove the OCT and finally redispersed by applying several 5 s ultrasonic pulses.

Characterization of MNPs and sMRFs: Transmission and scanning electron microscopy (TEM & SEM): The morphology and size of the designed MNPs were analyzed by TEM, using a Phillips CM-12 microscope operating with an acceleration voltage of 120 kV in a 100000X to 500000X magnification range. The samples were prepared by depositing 10 µL of diluted MNPs solutions in a copper TEM grid, which was subsequently dried under ambient conditions for 1 h. The microstructure of electrospun short microfibers was observed by high-resolution SEM (JSM-6010LV, JEOL). To prepare SEM samples, 20 µL of microfibers aqueous solutions were deposited on a glass slide and dried at room temperature for 24 h. The images were collected with an acceleration voltage from 2 to 10 kV.

X-Ray diffraction (XRD): XRD measurements were performed using a Phillips diffractometer equipped with a PW1710 control unit, a PW1820/00 vertical goniometer and an Enraf Nonius FR590 generator, operating at 40 kV and 30 mA. X-rays were obtained from a sealed copper tube and the radiation was treated with a graphite monochromator, using a PanAnalytical PIXcel-3 detector. The diffractograms were determined in the 10°-70° angular range, with pitch angle and time of 0.02° and 2 s, respectively. MNPs were dried for 24 h under 60 °C and 50 mbar conditions before measurements.

Inductively coupled plasma mass spectrometry (ICP-MS): MNPs composition and the amount of magnetic material incorporated in hybrid microfibers were determined by using an Agilent 7700xICP-MS equipped with a MicromistGlass low-flow nebulizer and a double pass glass spray chamber with Peltier system, operating with a power of 1550 W and a plasma flow of 15 dm³ min⁻¹. To prepare the samples, 20 µL of the analyzed solution were dissolved in 480 µL of a 75/25 (v/v) hydrochloric acid/nitric acid (Sigma–Aldrich) mixture and, after 2 h, 4.5 mL of nitric acid 1% were finally added.

Thermogravimetric analysis (TGA): The thermogravimetric characterization of the samples was carried out by using a TGA Q500 equipment, analyzing the temperature range from 20 to 500 °C (heating rate 10 °C min⁻¹). The samples were stabilized for 15 min. before performing the measurements, applying a nitrogen flow of 100 mL min⁻¹ during the experiments.

Superconducting quantum interference device (SQUID) magnetometry: the magnetic characterization of the designed systems was performed with a SQUID magnetometer (Quantum Design MPMS5, San Diego, CA). Magnetizations versus applied magnetic field curves were obtained from −4 T to + 4 T at 310 K. To prepare the samples, MNPs and sMRFs were freeze-dried for 24 h and then 5–6 mg of dried material were used for each measurement, normalizing the obtained magnetization values respect to the weight of MNPs/sMRFs.

Statistical size and inter-distances distributions: the statistical distributions of sizes of the different synthesized structures were determined using ImageJ software (National Institute of Health, USA), carrying out a minimum of 250 independent measurements for each distribution. The inter-distances between hybrid microfibers within polymeric hydrogels after their remote alignment were measured using this same tool. For this, the value of this inter-distance was considered as the separation between a fiber and its closest counterpart in the direction perpendicular to the alignment.

Magnetic Field Generation Setups: The magnetostatic fields applied to align the magnetically-responsive hybrid microfibers within the hydrogels were generated by using a two-parallel neodymium magnets system. This experimental setup allowed the generation of uniaxial magnetic fields with highly-uniform strength in a large region between the magnets. By using a gaussmeter, we measured that the created magnetostatic fields in the center point between the magnets can be adjusted by varying the inter-distance between them 14 ± 2 mT (magnets separated 5.1 cm) to 238 ± 15 mT (1.0 cm). In the magnetically-assisted 3D bioprinting processes, the magnetic setup was placed in the printing surface and the bioink extruded in the central plane between the magnets. The computational simulation of the magnetic field generated by parallel magnets setup was performed using COMSOL Multiphysics Software, v. 5.6.

For the magnetic stimulation of the cell-laden 3D bioprinted composites, a commercially-available horizontal oscillating magnetic bioreactor (nanoTherics Ltd, UK) generating 194 ± 13 mT magnetic field strengths was used with oscillation frequency and displacement of 2 Hz and 0.2 mm, respectively.[78,99,100] This setup was based on permanent magnets that generate magnetostatic fields, but their oscillation respect the position of the stimulated constructs induce changes on the magnetic field strength applied to the samples, being in fact an alternating magnetic stimulus.

Fabrication of Hydrogels Loaded with sMRFs: Hydrogels precursor solutions were prepared by dissolving 7.5% (w/v) GelMA in culture media for 1 h at 60 °C in the presence of 0.25% (w/v) lithium phenyl-2,4,6-trimethylbenzoylphosphinate photoinitiator (LAP, Sigma–Aldrich), and finally adjusting the pH to 7.4. Preliminary studies to establish the amount of magnetically-responsive fibers and the intensity of the applied magnetic fields required to provide hydrogels with anisotropic architectures were performed as follow: GelMA-LAP and microfibers solutions were mixed at 37 °C in the presence of an external magnetic field created by a two-parallel magnets system and exposed for 40 s to a 385 W cm⁻² UV light for crosslinking, resulting in 7.5% (w/v) GelMA hydrogels loaded with different concentrations of aligned microfibers. The intensity of magnetic fields required to induce the alignment of

**ADVANCED
SCIENCE NEWS**

www.advancedsciencenews.com

**ADVANCED
FUNCTIONAL
MATERIALS**

www.afm-journal.de

magnetic fibers was evaluated, as well as the effect of microfibers length, magnetic content and concentration in the fabricated scaffolds.

The fraction volumes occupied by the sMRFs in the 3D printed structures were analyzed by confocal laser scanning microscopy (Leica TCS SP8, Microsystems, Wetzlar, Germany). For that, acquired confocal *z*-stacks were reconstructed into 3D images and, after removing the residual fluorescence, the density of rhodamine-stained sMRFs was quantified by means of fluorescence intensity (percentage of red-emission pixels).

Rheological Characterization of GelMA-sMRFs Solutions and Hydrogels: Rheological experiments were performed using a stress-controlled rheometer (Anton Paar MCR 302). The viscosity of GelMA-based solutions was evaluated over a logarithmic ramp of shear from 2 to 200 Hz. All measurements were performed at 37 °C using a solvent trap to prevent dehumidification. A 25 mm parallel plate geometry set at 1 mm gap was used. On the other hand, the stiffness (storage modulus, G') and the viscous properties of crosslinked hydrogels were assessed by oscillatory frequency sweeps. GelMA blocks loaded with random and aligned (parallel to bottom plate) sMRFs were analyzed, using neat GelMA blocks as control. Samples were stabilized in PBS during a period of 48 h before measurements. In this case, the rheometer was fitted with a 25 mm sand-blasted parallel plate upper geometry for better contact with the samples. The storage modulus was recorded over one decade of angular frequency from 0.2 to 2 Hz, applying an initial preadjusted normal force of 1 N and constant strain amplitude of 0.5%. According to ASTM D7175 and DIN 51810–2, the point where G' deviates more than a 10% from the initial plateau, indicates that the system was no longer working with a linear viscoelastic behavior. Dynamic amplitude sweeps were previously performed in order to assure that all the tests were carried out in this linear viscoelastic region.

Cells Isolation and Culture: hASCs were obtained from lipoaspirate samples of the abdominal region after informed consent of patients undergoing liposuction surgery, following the protocols established with Hospital da Prelada (Porto, Portugal) with the approval of the Hospital and University of Minho Ethics Committees (approval numbers 005/2019 and 014/2019, respectively). hASCs were isolated according to the previously optimized protocol.[101,102] Alpha modified Eagle medium supplemented with 10% (v/v) fetal bovine serum and 1% (v/v) penicillin/streptomycin solution was used to culture and expand the cells. The cells were not used beyond passage 8.

Magnetically-Assisted 3D Bioprinting of Cell-Laden Hydrogel Constructs Incorporating sMRFs: Support baths based on CNCs and agarose microparticles were evaluated. Colloidal suspensions of CNCs were produced by the hydrolysis of microcrystalline cellulose (Sigma–Aldrich) following previously reported protocols.[35,103] The CNCs fluid gel printing bath was prepared by adding calcium chloride (2 mᴍ; Sigma–Aldrich) to 2.5% (w/v) CNCs suspension. This mixture was sonicated for 1 min. at 40% amplitude output to ensure the homogeneity of the support bath. On the other hand, the agarose bath was produced by autoclaving 0.5% (w/v) agarose (SeaKem) with 14 mᴍ calcium chloride followed by cooling under 700 rpm magnetic stirring to form agarose microparticles. BioX (Cellink, Sweden) with a mechanical printhead was used for 3D (bio) printing experiments. Computer-aided designs (CAD) were created using the free online software TINKERCAD and saved in .stl (stereolithography) file format. The .stl to G-code conversion program PursaSlic3r 2.1 software was then used to slice the models into layers and translate the coordinates into commands. The inks were prepared by mixing GelMA-LAP solutions and sMRFs, resulting in final inks with GelMA concentration of 7.5% (w/v) with 0.25% (w/v) LAP. In the case of bioink, hASCs were suspended in the polymeric solutions at a cell density of 2×10^6 cells mL^{-1}. Cartridges of 3 mL were loaded with (bio)inks and 22G (0.41 mm inner diameter) blunt needles were used as nozzles. The prints were performed under 2.2 µL min^{-1} flow rate and 14 mm s^{-1} speed, using cell culture µ-dish plates (Ibidi, Germany) as support platforms for the prints.

For the magnetic setup, a poly-lactic acid (PLA, Mitsubishi Chemicals Performance Polymers, USA) mold was 3D printed in a B2×300 3D printer (Beeverycreative, Portugal) after preparing a CAD design with the dimensions required to place parallel neodymium magnets 5.1 cm apart within the printing platform, creating 14 ± 2 mT magnetic fields. The dishes with the support printing baths were placed in the center region between the magnets, thus ensuring a fairly uniform magnetic actuation over all the 3D (bio)printed composites. After construct printing, it was photocrosslinked with a 385 W cm^{-2} UV light with 4 cm distance between the light source and the printed scaffold. Next, the printed structure in CNC fluid gel was locked by addition of an excess of 7.5 mᴍ calcium chloride solution on the top of the constructs, which was replaced by culture media before placing the bioprinted constructs in the incubator. The fabricated tissue composites were cultured up to 4 weeks under standard culture condition (alpha-MEM with 10% FBS). For the magneto-mechanical stimulation of the cell-laden composites, they were placed on the top of the commercially-available horizontal oscillating magnetic bioreactor (described in section 4), which was arranged inside the incubator throughout the time of cell culture. The media was changed every alternate day.

Fluorescence Stainings of 3D Bioprinted Constructs: Cell viability was assessed by staining cells with Calcein AM (Thermo Fisher Scientific) 1:500 dilution in culture media and propidium iodide (Thermo Fisher Scientific) 1:1000 dilution in PBS for 30 min. on days 1, 3, 10, and 21. For immunostaining, the cells were fixed with 4% paraformaldehyde (Thermo Fisher Scientific) at room temperature for 30 min. Then 0.2% Triton X-100 in PBS was used to permeabilize the cell membrane for 1 h at room temperature under gentle agitation. Next, the samples were blocked with 3% (w/v) BSA in 0.2% (w/v) Triton X-100 in PBS for 1 h. After washing the samples three times with PBS they were incubated with primary antibody against YAP1 (Santa Cruz Biotechnology 1:200) or TNMD (abcam 1:200), diluted in 1% (w/v) BSA in 0.2% (w/v) Triton X-100 in PBS at 4 °C over night with gentle agitation. This was followed by incubation for 1 more day at 4 °C with the respective AlexaFluor-488 secondary antibodies. Cytoskeleton and nuclei were stained with DAPI and Phalloidin for 1 h (DAPI, Sigma–Aldrich, 1:1000 dilution; Phalloidin conjugated with rhodamine, Sigma–Aldrich, 1:200 dilution). Samples were analyzed by confocal laser scanning microscopy. We calculated the nuclear (delimited by the DAPI staining) YAP/TAZ intensity for each cell in static and stimulated cells using Image J (National Institute of Health, USA). All the results are provided as mean ± standard deviation (n = 3, independent experiments).

mRNA Extraction and Real-Time RT-PCR: Total RNA was extracted from the constructs using Trizol extraction reagent (TRI Reagent-T9424Sigma Life Science) according to the manufacturer's instructions. The quantity and quality of extracted RNA was analyzed with NanoDrop ND-1000 spectrophotometer (NanoDrop, ThermoScientific, USA). The cDNA synthesis was performed by qScript cDNA SuperMix kit (Thermo Fisher Scientific). The quantitative polymerase chain reaction (qPCR) was carried out for the quantification of the transcripts using the PerfeCTASYBR Green FastMix kit following the manufacturer's protocol, in a Real-Time Mastercycler Realplex thermocycler (Eppendorf, Germany). The primers were pre-designed with Primer3 and BLAST (NCBI, Bethesda, MD, USA) (Table S7, Supporting Information). GAPDH (Glyceraldehyde 3-phosphate dehydrogenase) was used as the reference gene. The Delta-Delta Ct Method was selected to evaluate the relative expression level for each target gene. All values were first normalized against GAPDH values, and then to hASCs collected immediately after printing (day 0; n = 3, independent experiments).

Statistical Analysis: GraphPad Prism 6 software was used for the statistical analysis. For the analysis of variance between multiple groups Two-way ANOVA followed by Tukey's post hoc tests was used. To compare between two experimental groups unpaired two-tailed Student's *t*-tests with Welch's correction was used. Results are provided as mean ± standard deviation of n ≥ 3 independent experiments. Values were considered significant when $p < 0.05$.

Supporting Information

Supporting Information is available from the Wiley Online Library or from the author.

Conflict of Interest

The authors declare no conflict of interest.

Data Availability Statement

The data that support the findings of this study are available from the corresponding author upon reasonable request.

[1] C. Leclech, A. I. Barakat, *Cytoskeleton* **2021**, *78*, 284.

[2] J. L. Funnell, A. M. Ziemba, J. F. Nowak, H. Awada, N. Prokopiou, J. Samuel, Y. Guari, B. Nottelet, R. J. Gilbert, *Acta Biomater.* **2021**, *131*, 302.

[3] M. Tadsen, R. P. Friedrich, S. Riedel, C. Alexiou, S. G. Mayr, *ACS Appl. Mater. Interfaces* **2019**, *11*, 7450.

[4] A. Sivashanmugam, R. Arun Kumar, M. Vishnu Priya, S. V. Nair, R. Jayakumar, *Eur. Polym. J.* **2015**, *72*, 543.

[5] S. Van Vlierberghe, P. Dubruel, E. Schacht, *Biomacromolecules* **2011**, *12*, 1387.

[6] J. Xing, N. Liu, N. Xu, W. Chen, D. Xing, *Adv. Funct. Mater.* **2022**, *32*, 2110676.

[7] S. Jana, S. K. L. Levengood, M. Zhang, *Adv. Mater.* **2016**, *28*, 10588.

[8] G. Z. Tan, Y. Zhou, *Int. J. Polym. Mater. Polym. Biomater.* **2019**, *69*, 947.

[9] M. Chau, K. J. De France, B. Kopera, V. R. Machado, S. Rosenfeldt, L. Reyes, K. J. W. Chan, S. Förster, E. D. Cranston, T. Hoare, E. Kumacheva, *Chem. Mater.* **2016**, *28*, 3406.

[10] X. Y. Lin, Z. J. Wang, P. Pan, Z. L. Wu, Q. Zheng, *RSC Adv.* **2016**, *6*, 95239.

[11] Q. Lu, S. Bai, Z. Ding, H. Guo, Z. Shao, H. Zhu, D. L. Kaplan, *Adv. Mater. Interfaces* **2016**, *3*, 1500687.

[12] N. Wang, M. Ma, Y. Luo, T. Liu, P. Zhou, S. Qi, Y. Xu, H. Chen, *ChemNanoMat* **2018**, *4*, 631.

[13] C. Di Meo, T. Coviello, P. Matricardi, F. Alhaique, D. Capitani, R. Lamanna, *Soft Matter* **2011**, *7*, 6068.

[14] Z. L. Wu, T. Kurokawa, D. Sawada, J. Hu, H. Furukawa, J. P. Gong, *Macromolecules* **2011**, *44*, 3535.

[15] N. D. Dinh, R. Luo, M. T. A. Christine, W. N. Lin, W. C. Shih, J. C. H. Goh, C. H. Chen, *Small* **2017**, *13*, 1700684.

[16] A. Pardo, M. Gómez-Florit, S. Barbosa, P. Taboada, R. M. A. Domingues, M. E. Gomes, *ACS Nano* **2021**, *15*, 175.

[17] M. Filippi, B. Dasen, J. Guerrero, F. Garello, G. Isu, G. Born, M. Ehrbar, I. Martin, A. Scherberich, *Biomaterials* **2019**, *223*, 119468.

[18] R. Fuhrer, S. Hofmann, N. Hild, J. R. Vetsch, I. K. Herrmann, R. N. Grass, W. J. Stark, *PLoS One* **2013**, *8*, e81362.

[19] A. Tay, A. Sohrabi, K. Poole, S. Seidlits, D. Di Carlo, *Adv. Mater.* **2018**, *30*, 1800927.

[20] S. M. Bakht, A. Pardo, M. Gómez-Florit, R. L. Reis, R. M. A. Domingues, M. E. Gomes, *J. Mater. Chem. B* **2021**, *9*, 5025.

[21] R. Tognato, A. R. Armiento, V. Bonfrate, R. Levato, J. Malda, M. Alini, D. Eglin, G. Giancane, T. Serra, *Adv. Funct. Mater.* **2019**, *29*, 1804647.

[22] M. Betsch, C. Cristian, Y. Y. Lin, A. Blaeser, J. Schöneberg, M. Vogt, E. M. Buhl, H. Fischer, D. F. Duarte Campos, *Adv. Healthcare Mater.* **2018**, *7*, 1800894.

[23] A. Omidinia-Anarkoli, S. Boesveld, U. Tuvshindorj, J. C. Rose, T. Haraszti, L. De Laporte, *Small* **2017**, *13*, 1702207.

[24] S. Araújo-Custódio, M. Gomez-Florit, A. R. Tomás, B. B. Mendes, P. S. Babo, S. M. Mithieux, A. Weiss, R. M. A. Domingues, R. L. Reis, M. E. Gomes, *ACS Biomater. Sci. Eng.* **2019**, *5*, 1392.

[25] J. E. Bae, M. Il Huh, B. K. Ryu, J. Y. Do, S. U. Jin, M. J. Moon, J. C. Jung, Y. Chang, E. Kim, S. G. Chi, G. H. Lee, K. S. Chae, *Biomaterials* **2011**, *32*, 9401.

[26] N. Malhotra, J. S. Lee, R. A. D. Liman, J. M. S. Ruallo, O. B. Villaflore, T. R. Ger, C. D. Hsiao, *Molecules* **2020**, *25*, 3159.

[27] X. Zhang, K. Yarema, A. Xu, In *Biological Effects of Static Magnetic Fields*, Springer, Singapore, **2017**, pp. 3.

[28] D. Kokkinis, M. Schaffner, A. R. Studart, *Nat. Commun.* **2015**, *6*, 8643.

[29] W. Xu, S. Jambhulkar, D. Ravichandran, Y. Zhu, M. Kakarla, Q. Nian, B. Azeredo, X. Chen, K. Jin, B. Vernon, D. G. Lott, J. L. Cornella, O. Shefi, G. Miquelard-Garnier, Y. Yang, K. Song, *Small* **2021**, *17*, 2100817.

[30] Y. Ma, Q. Wu, L. Duanmu, S. Wu, Q. Liu, B. Li, X. Zhou, *J. Mater. Sci.* **2020**, *55*, 15510.

[31] B. B. Mendes, M. Gómez-Florit, A. G. Hamilton, M. S. Detamore, R. M. A. Domingues, R. L. Reis, M. E. Gomes, *Biofabrication* **2020**, *12*, 015012.

[32] J. J. Senior, M. E. Cooke, L. M. Grover, A. M. Smith, *Adv. Funct. Mater.* **2019**, *29*, 1904845.

[33] S. R. Moxon, M. E. Cooke, S. C. Cox, M. Snow, L. Jeys, S. W. Jones, A. M. Smith, L. M. Grover, *Adv. Mater.* **2017**, *29*, 1605594.

[34] A. Lee, A. R. Hudson, D. J. Shiwarski, J. W. Tashman, T. J. Hinton, S. Yerneni, J. M. Bliley, P. G. Campbell, A. W. Feinberg, *Science* **2019**, *365*, 482.

[35] S. M. Bakht, M. Gomez-Florit, T. Lamers, R. L. Reis, R. M. A. Domingues, M. E. Gomes, *Adv. Funct. Mater.* **2021**, *31*, 2104245.

[36] A. Pardo, B. Pelaz, J. Gallo, M. Bañobre-López, W. J. Parak, S. Barbosa, P. del Pino, P. Taboada, *Chem. Mater.* **2020**, *32*, 2220.

[37] A. Pardo, S. Yáñez, Y. Piñeiro, R. Iglesias-Rey, A. Al-Modlej, S. Barbosa, J. Rivas, P. Taboada, *ACS Appl. Mater. Interfaces* **2020**, *12*, 9017.

[38] P. Guardia, R. Di Corato, L. Lartigue, C. Wilhelm, A. Espinosa, M. Garcia-Hernandez, F. Gazeau, L. Manna, T. Pellegrino, *ACS Nano* **2012**, *6*, 3080.

**ADVANCED
SCIENCE NEWS**

www.advancedsciencenews.com

**ADVANCED
FUNCTIONAL
MATERIALS**

www.afm-journal.de

[39] D. Caruntu, G. Caruntu, C. J. O'Connor, *J Phys D Appl Phys* **2007**, *40*, 5801.

[40] Q. Li, C. W. Kartikowati, S. Horie, T. Ogi, T. Iwaki, K. Okuyama, *Sci. Rep.* **2017**, *7*, 9894.

[41] P. Thakur, D. Chahar, S. Taneja, N. Bhalla, A. Thakur, *Ceram. Int.* **2020**, *46*, 15740.

[42] A. G. Kolhatkar, A. C. Jamison, D. Litvinov, R. C. Willson, T. R. Lee, *Int. J. Mol. Sci.* **2013**, *14*, 15977.

[43] M. Darbandi, F. Stromberg, J. Landers, N. Reckers, B. Sanyal, W. Keune, H. Wende, *J Phys D Appl Phys* **2012**, *45*, 195001.

[44] J. M. Byrne, V. S. Coker, E. Cespedes, P. L. Wincott, D. J. Vaughan, R. A. D. Pattrick, G. Van Der Laan, E. Arenholz, F. Tuna, M. Bencsik, J. R. Lloyd, N. D. Telling, *Adv. Funct. Mater.* **2014**, *24*, 2518.

[45] S. H. Noh, W. Na, J. T. Jang, J. H. Lee, E. J. Lee, S. H. Moon, Y. Lim, J. S. Shin, J. Cheon, *Nano Lett.* **2012**, *12*, 3716.

[46] O. Karovic, I. Tonazzini, N. Rebola, E. Edström, C. Lövdahl, B. B. Fredholm, E. Daré, *Biochem. Pharmacol.* **2007**, *73*, 694.

[47] S. Zhu, X. Xu, R. Rong, B. Li, X. Wang, *Toxicol. Res. (Camb).* **2015**, *5*, 97.

[48] R. Sakai, Y. Teramoto, Y. Nishio, *Polym J* **2018**, *50*, 251.

[49] N. A. Jalili, M. Muscarello, A. K. Gaharwar, *Bioeng. Transl. Med.* **2016**, *1*, 297.

[50] M. Blank, R. Goodman, *Pathophysiology* **2009**, *16*, 71.

[51] J. C. Rose, M. Cámara-Torres, K. Rahimi, J. Köhler, M. Möller, L. De Laporte, *Nano Lett.* **2017**, *17*, 3782.

[52] M. R. Sommer, R. M. Erb, A. R. Studart, *ACS Appl. Mater. Interfaces* **2012**, *4*, 5086.

[53] M. D. Davidson, M. E. Prendergast, E. Ban, K. L. Xu, G. Mickel, P. Mensah, A. Dhand, P. A. Janmey, V. B. Shenoy, J. A. Burdick, *Sci. Adv.* **2021**, *7*, 8157.

[54] A. D. Doyle, N. Carvajal, A. Jin, K. Matsumoto, K. M. Yamada, *Nat. Commun.* **2015**, *6*, 8720.

[55] A. McCormack, C. B. Highley, N. R. Leslie, F. P. W. Melchels, *Trends Biotechnol.* **2020**, *38*, 584.

[56] R. Sobreiro-Almeida, M. Gómez-Florit, R. Quinteira, R. L. Reis, M. E. Gomes, N. M. Neves, *Biofabrication* **2021**, *13*, 045006.

[57] E. Mirdamadi, N. Muselimyan, P. Koti, H. Asfour, N. Sarvazyan, *3D Print. Addit. Manuf.* **2019**, *6*, 158.

[58] M. E. Prendergast, M. D. Davidson, J. A. Burdick, *Biofabrication* **2021**, *13*, 044108.

[59] B. Velasco-Rodriguez, T. Diaz-vidal, L. C. Rosales-rivera, C. A. García-gonzález, C. Alvarez-lorenzo, A. Al-modlej, V. Domínguez-arca, G. Prieto, S. Barbosa, J. F. A. Soltero Martínez, P. Taboada, *Int. J. Mol. Sci.* **2021**, *22*, 6758.

[60] M. Antman-Passig, O. Shefi, *Nano Lett.* **2016**, *16*, 2567.

[61] P. Ghaderinejad, N. Najmoddin, Z. Bagher, M. Saeed, S. Karimi, S. Simorgh, M. Pezeshki-Modaress, *Chem. Eng. J.* **2021**, *420*, 130465.

[62] H. L. Hiraki, D. L. Matera, M. J. Rose, R. N. Kent, C. W. Todd, M. E. Stout, A. E. Wank, M. C. Schiavone, S. J. DePalma, A. A. Zarouk, B. M. Baker, *Front Bioeng. Biotechnol.* **2021**, *9*, 679165.

[63] R. Dai, Z. Wang, R. Samanipour, K. I. Koo, K. Kim, *Stem Cells Int* **2016**, *2016*, 6737345.

[64] A. Abaci, M. Guvendiren, *Adv. Healthcare Mater.* **2020**, *9*, 2000734.

[65] M. M. Smoak, K. J. Hogan, K. J. Grande-Allen, A. G. Mikos, *Sci. Adv.* **2021**, *7*, abg4143.

[66] T. Tu, Y. Shen, X. Wang, W. Zhang, G. Zhou, Y. Zhang, W. Wang, W. Liu, *Appl. Mater. Today* **2020**, *18*, 100495.

[67] S. Gao, W. Guo, M. Chen, Z. Yuan, M. Wang, Y. Zhang, S. Liu, T. Xi, Q. Guo, *J. Mater. Chem. B* **2017**, *5*, 2273.

[68] C. Dong, F. Qiao, G. Chen, Y. Lv, *J. Mater. Chem. B* **2021**, *9*, 6881.

[69] D. L. Matera, K. M. DiLillo, M. R. Smith, C. D. Davidson, R. Parikh, M. Said, C. A. Wilke, I. M. Lombaert, K. B. Arnold, B. B. Moore, B. M. Baker, *Sci. Adv.* **2020**, *6*, eabb5069.

[70] J. C. Rose, D. B. Gehlen, T. Haraszti, J. Köhler, C. J. Licht, L. De Laporte, *Biomaterials* **2018**, *163*, 128.

[71] D. L. Jones, R. N. Daniels, X. Jiang, R. C. Locke, M. K. Evans, E. D. Bonnevie, A. Srikumar, M. P. Nijsure, J. D. Boerckel, R. L. Mauck, N. A. Dyment, *bioRxiv* **2022**, *7*, 499650.

[72] R. Sheng, Y. Jiang, L. J. Backman, W. Zhang, J. Chen, *Stem Cells Int* **2020**, *2020*, 8824783.

[73] N. R. Schiele, J. E. Marturano, C. K. Kuo, *Curr. Opin. Biotechnol.* **2013**, *24*, 834.

[74] A. Totaro, T. Panciera, S. Piccolo, *Nat. Cell Biol.* **2018**, *20*, 888.

[75] C. L. Happe, A. J. Engler, *Circ. Res.* **2016**, *118*, 296.

[76] A. Totaro, M. Castellan, G. Battilana, F. Zanconato, L. Azzolin, S. Giulitti, M. Cordenonsi, S. Piccolo, *Nat. Commun.* **2017**, *8*, 15206.

[77] S. Dupont, L. Morsut, M. Aragona, E. Enzo, S. Giulitti, M. Cordenonsi, F. Zanconato, J. L.e Digabel, M. Forcato, S. Bicciato, N. Elvassore, S. Piccolo, *Nature* **2011**, *474*, 179.

[78] A. R. Tomás, A. I. Gonçalves, E. Paz, P. Freitas, R. M. A. Domingues, M. E. Gomes, *Nanoscale* **2019**, *11*, 18255.

[79] L. Zheng, L. Zhang, L. Chen, J. Jiang, X. Zhou, M. Wang, Y. Fan, *J. Tissue Eng. Regener. Med.* **2018**, *12*, 1432.

[80] I. Dasgupta, D. McCollum, *J. Biol. Chem.* **2019**, *294*, 17693.

[81] Y. Xu, H. Yin, J. Chu, D. Eglin, T. Serra, D. Docheva, *Biomater. Sci.* **2021**, *9*, 1237.

[82] I. Calejo, C. J. Labrador-Rached, M. Gomez-Florit, D. Docheva, R. L. Reis, R. M. A. Domingues, M. E. Gomes, *Adv. Healthcare Mater.* **2022**, *11*, 2102863.

[83] M. Gomez-Florit, C. J. Labrador-Rached, R. M. A. Domingues, M. E. Gomes, *Adv. Drug Delivery Rev.* **2022**, *185*, 114299.

[84] C. Shukunami, A. Takimoto, Y. Nishizaki, Y. Yoshimoto, S. Tanaka, S. Miura, H. Watanabe, T. Sakuma, T. Yamamoto, G. Kondoh, Y. Hiraki, *Sci. Rep.* **2018**, *8*, 3155.

[85] T. W. Qin, Y. L. Sun, A. R. Thoreson, S. P. Steinmann, P. C. Amadio, K. N. An, C. Zhao, *Biomaterials* **2015**, *51*, 43.

[86] H. R. C. Screen, D. E. Berk, K. E. Kadler, F. Ramirez, M. F. Young, *J Orthop Res* **2015**, *33*, 793.

[87] C. Rinoldi, M. Costantini, E. Kijeńska-Gawrońska, S. Testa, E. Fornetti, M. Heljak, M. Ćwiklińska, R. Buda, J. Baldi, S. Cannata, J. Guzowski, C. Gargioli, A. Khademhosseini, W. Swieszkowski, *Adv. Healthcare Mater.* **2019**, *8*, 1801218.

[88] S. K. Theodossiou, N. R. Schiele, *BMC Biomed Eng* **2019**, *1*, 32.

[89] S. L. Wunderli, U. Blache, J. G. Snedeker, *Connect. Tissue Res.* **2020**, *61*, 262.

[90] I. V. Belyanina, T. N. Zamay, G. S. Zamay, S. S. Zamay, O. S. Kolovskaya, T. I. Ivanchenko, V. V. Denisenko, A. K. Kirichenko, Y. E. Glazyrin, I. V. Garanzha, V. V. Grigorieva, A. V. Shabanov, D. V. Veprintsev, A. E. Sokolov, V. M. Sadovskii, A. Gargaun, M. V. Berezovski, A. S. Kichkailo, *Theranostics* **2017**, *7*, 3326.

[91] R. Chen, G. Romero, M. G. Christiansen, A. Mohr, P. Anikeeva, *Science* **2015**, *347*, 1477.

[92] J. Yao, C. Yao, A. Zhang, X. Xu, A. Wu, F. Yang, *J. Mater. Chem. B* **2022**, *10*, 7136.

[93] T. Nguyen, J. Gao, P. Wang, A. Nagesetti, P. Andrews, S. Masood, Z. Vriesman, P. Liang, S. Khizroev, X. Jin, *Neurotherapeutics* **2021**, *18*, 2091.

[94] S. Testa, M. Costantini, E. Fornetti, S. Bernardini, M. Trombetta, D. Seliktar, S. Cannata, A. Rainer, C. Gargioli, *J. Cell. Mol. Med.* **2017**, *21*, 2711.

[95] C. Rinoldi, A. Fallahi, I. K. Yazdi, J. Campos Paras, E. Kijeńska-Gawrońska, G. Trujillo-De Santiago, A. Tuoheti, D. Demarchi, N. Annabi, A. Khademhosseini, W. Swieszkowski, A. Tamayol, *ACS Biomater. Sci. Eng.* **2019**, *5*, 2953.

[96] H. Yin, F. Strunz, Z. Yan, J. Lu, C. Brochhausen, S. Kiderlen, H. Clausen-Schaumann, X. Wang, M. E. Gomes, V. Alt, D. Docheva, *Biomaterials* **2020**, *236*, 119802.

[97] D. Wang, Z. L. Ji, J. M. Wang, Y. Y. Tan, *Exp Ther Med* **2018**, *16*, 5067.

[98] K. M. Hirpara, O. Abouazza, B. O'Neill, M. O'Sullivan, *J Musculoskelet Res* **2006**, *10*, 181.

[99] A. I. Gonçalves, M. Rotherham, H. Markides, M. T. Rodrigues, R. L. Reis, M. E. Gomes, A. J. El Haj, *Nanomedicine* **2018**, *14*, 1149.

[100] A. I. Gonçalves, M. T. Rodrigues, M. E. Gomes, *Acta Biomater.* **2017**, *63*, 110.

[101] P. P. Carvalho, X. Wu, G. Yu, I. R. Dias, M. E. Gomes, R. L. Reis, J. M. Gimble, *Cells Tissues Organs* **2011**, *194*, 494.

[102] G. Yu, Z. E. Floyd, X. Wu, Y. D. C. Halvorsen, J. M. Gimble, *Methods Mol Biol* **2011**, *702*, 17.

[103] H. G. Yi, Y. H. Jeong, Y. Kim, Y. J. Choi, H. E. Moon, S. H. Park, K. S. Kang, M. Bae, J. Jang, H. Youn, S. H. Paek, D. W. Cho, *Nat. Biomed. Eng.* **2019**, *3*, 509.